

The Cosmic Lens All-Sky Survey: statistical strong lensing, cosmological parameters, and global properties of galaxy populations

Kyu-Hyun Chae

Sejong University, Department of Astronomy and Space Sciences, 98 Gunja-dong, Gwangjin-Gu, Seoul 143-747, Republic of Korea; University of Manchester, Jodrell Bank Observatory, Macclesfield, Cheshire SK11 9DL, UK

Accepted Received; in original form

ABSTRACT

Extensive analyses of statistical strong gravitational lensing are performed based on the final Cosmic Lens All-Sky Survey (CLASS) well-defined statistical sample of flat-spectrum radio sources and current estimates of galaxy luminosity functions per morphological type. The analyses are done under the assumption that galactic lenses are well-approximated by singular isothermal ellipsoids and early-type galaxies evolved passively since redshift $z \sim 1$. Two goals of the analyses are: (1) to constrain cosmological parameters independently of other techniques (e.g. Type Ia supernovae magnitude-redshift relation, cosmic microwave background anisotropies, galaxy matter power spectra); and (2) to constrain the characteristic line-of-sight velocity dispersion and the mean projected mass ellipticity for the early-type galaxy population. Depending on how the late-type galaxy population is treated (i.e., whether its characteristic velocity dispersion is constrained or not), we find for a flat universe with a classical cosmological constant that the matter fraction of the present critical density $\Omega_m = 0.31^{+0.27}_{-0.14}$ (68%) for the unconstrained case or $0.40^{+0.28}_{-0.16}$ (68%) for the constrained case, with an additional systematic uncertainty of ≈ 0.11 arising from the present uncertainty in the distribution of CLASS sources in redshift and flux density. For a flat universe with a constant equation of state for dark energy $w = p_x(\text{pressure})/\rho_x(\text{energy density})$ and the prior constraint $w \geq -1$, we find that $-1 \leq w < -0.55^{+0.18}_{-0.11}$ (68%) for the unconstrained case or $-1 \leq w < -0.41^{+0.28}_{-0.16}$ (68%) for the constrained case, where $w = -1$ corresponds to a classical cosmological constant. The determined value of the early-type characteristic velocity dispersion ($\sigma_*^{(e)}$) depends on the faint-end slope of the early-type luminosity function ($\alpha^{(e)}$) and the intrinsic shape distribution of galaxies; for equal frequencies of oblates and prolates, we find that $\sigma_*^{(e)}(0.3 \lesssim z \lesssim 1) = 198^{+22}_{-18}$ km s $^{-1}$ (68%) for a ‘steep’ $\alpha^{(e)} = -1$ or $\sigma_*^{(e)}(0.3 \lesssim z \lesssim 1) = 181^{+18}_{-15}$ km s $^{-1}$ (68%) for a ‘shallow’ $\alpha^{(e)} = -0.54$. Finally, from the relative frequencies of doubly-imaged sources and quadruply-imaged sources, we find that a mean projected mass ellipticity of early-type galaxies $\bar{\epsilon}_{\text{mass}} = 0.42$ with a 68% lower limit of 0.28 assuming equal frequencies of oblates and prolates.

Key words: gravitational lensing - cosmological parameters - galaxies: structure - galaxies: kinematics and dynamics - galaxies: halos - methods: statistical

1 INTRODUCTION

Analysing the statistical properties of strong gravitational lensing in a sample of cosmologically distant sources provides a method for constraining cosmological parameters (e.g. Turner 1990; Fukugita, Futamase, & Kasai 1990; Fukugita & Turner 1991; Fukugita et al. 1992; Carroll, Press, & Turner 1992) as well as for constraining global proper-

ties of galaxy populations including evolutions (e.g. Maoz & Rix 1993; Kochanek 1993; Mao & Kochanek 1994; King & Browne 1996). The observed statistical properties of gravitational lensing in a sample are the total rate of multiple-imaging, the image separations, the lens redshifts, the source redshifts, and the image multiplicities. These properties depend not only on cosmological parameters but also on the following properties of galaxies and sources (e.g. Turner, Os-

arXiv:astro-ph/0211244v2 18 Aug 2003

triker, & Gott 1984; Turner 1990; Fukugita & Turner 1991; Mao 1991; Kochanek 1993; Maoz & Rix 1993; Wallington & Narayan 1993; Mao & Kochanek 1994; King & Browne 1996; Kochanek 1996a,b): (1) the galaxy luminosity functions per morphological type (and their evolutions of any relevance to lensing) and the projected mass distribution in the inner cylindrical region of a galaxy of given luminosity and morphological type; and (2) the distribution of the sources in redshift and flux in the observational selection waveband (e.g. radio). Because of the dependences of the statistical properties of gravitational lensing on the above multiple factors, analyses of statistical lensing can be used for various purposes. On the other hand, in order to derive reliable results from an analysis of statistical lensing, it is vital to properly take into account all the factors through a statistical lensing model based on reliable data.

In this paper we perform extensive analyses of statistical lensing based on more reliable sets of data than were available previously and using a more realistic statistical lensing model. Essential results on cosmological parameters from (part of) the analyses are reported in Chae et al. (2002). However, in this paper we present not only the details of the analyses but also comprehensive results of the analyses for a broader range of parameters. In particular, we derive and discuss the global properties of the galaxies. In comparison to previous works on statistical lensing that attempted to put limits on cosmological parameters (e.g. Kochanek 1996a; Falco, Kochanek, & Muñoz 1998; Chiba & Yoshii 1999; Helbig et al. 1999; Cooray 1999), the following aspects of this work can be pointed out:

(i) This work is based on the final Cosmic Lens All-Sky Survey (CLASS: Myers et al. 2003; Browne et al. 2003) statistical sample of 8958 radio sources [which includes Jodrell-Bank-VLA Astrometric Survey (JVAS) sources as a sub-sample] containing 13 multiply-imaged sources, which is the largest statistical sample that satisfies well-defined observational selection criteria.

(ii) This work is based on estimates of luminosity functions of galaxies per morphological type that have been derived taking into account latest results from large-scale observations of galaxies particularly including the Two Degree Field Galaxy Redshift Survey (2dFGRS) and the Sloan Digital Sky Survey (SDSS).

(iii) We adopt a statistical lensing model in which we not only use elliptical projected densities for galaxies but also incorporate intrinsic shapes of galaxies. The adopted galactic model is the axisymmetric (i.e. oblate and prolate) singular isothermal ellipsoid (SIE) with a distribution function of the form $\mathcal{F} = \mathcal{F}(E, L_z)$, where E and L_z are respectively the relative energy and the angular momentum component parallel to the symmetry axis.

(iv) This work is intended to provide robust constraints in cosmological parameter space. We make the least possible prior assumptions on the parameters of the assumed statistical lensing model and constrain the parameters self-consistently from the data of statistical lensing.

(v) This work is intended to be an investigation of global properties of galaxy populations; namely, characteristic velocity dispersion(s) for the early-type (and the late-type) galaxy population(s), mean apparent mass axial ratio of galaxies, and intrinsic shapes of galaxies. These investiga-

tions are made possible by the use of the (3-dimensional) ellipsoidal lens model [the above point (iii)].

This paper is organized as follows. In section 2, we build up the statistical lensing model based on the singular isothermal ellipsoid (SIE) mass model for a galaxy, including the calculation of the cross sections for double-imaging and quadruple-imaging as functions of line-of-sight velocity dispersion, apparent ellipticity and assumed intrinsic shape distributions, and the calculation of magnification biases for double-imaging and quadruple-imaging. In section 2, we also define the likelihood function for the data given the model of statistical lensing. In section 3, we summarize the input data for the analyses including the final CLASS statistical sample, distribution of the CLASS sources in redshift and radio flux density, and galaxy luminosity functions per morphological type. The results of fitting the model to the data are presented in section 4. In section 5, we discuss the derived results including comparison with previous results from statistical lensing and examination of possible systematics that could affect the derived results. In section 6, we discuss future prospects of statistical lensing. Conclusions are given in section 7.

2 MODEL AND METHOD

2.1 Lens model: the singular isothermal ellipsoid

The isothermal mass profile (i.e. the density $\rho \sim r^{-2}$) has been widely used for analyses of statistical lensing (e.g. Turner, Ostriker, & Gott 1984; Fukugita & Turner 1991; Kochanek 1993; Maoz & Rix 1993; Wallington & Narayan 1993; Mao & Kochanek 1994; King & Browne 1996; Kochanek 1996a,b; Falco, Kochanek, & Muñoz 1998; Chiba & Yoshii 1999; Helbig et al. 1999; Cooray 1999; Rusin & Tegmark 2001), because of the analytical tractability of the isothermal profile and because the projected surface density of the inner cylindrical regions of lensing galaxies probed by strong gravitational lensing are either consistent with or not too different from the isothermal profile.¹ Isothermal mass models would, in general, be too simplified to allow us to do accurate modelling of individual lenses (see, e.g., Muñoz, Kochanek, & Keeton 2001; Chae 2002), but they should suffice at least as first-order approximations to the mean properties of galaxies relevant to statistical lensing. Thus, following the literature on statistical lensing, we adopt the isothermal mass profile for our analyses. However, we use a more general isothermal model that incorporates not only a galaxy's apparent axial ratio but also its intrinsic shape.²

¹ The reader is referred to numerous examples in the literature [see, e.g., Treu & Koopmans (2002) and Koopmans & Treu (2003) for very recent examples].

² All the previous works on statistical lensing that intended to put limits on cosmological parameters used an isothermal sphere, while the works that focused on studying the relative frequencies of image multiplicities used an elliptical lens model (e.g. King & Browne 1996; Kochanek 1996b; Rusin & Tegmark 2001).

2.1.1 The surface density, dynamical normalisations, and cross sections

The projected surface density of the SIE lens $\Sigma^{\text{SIE}}(x, y)$ can be written in units of the critical surface density Σ_{cr} by

$$\begin{aligned} \kappa^{\text{SIE}}(x, y) &\equiv \frac{1}{\Sigma_{\text{cr}}} \Sigma^{\text{SIE}}(x, y) \\ &\equiv \frac{4\pi G}{c^2} R_H \frac{\hat{D}(0, z_l) \hat{D}(z_l, z_s)}{\hat{D}(0, z_s)} \Sigma^{\text{SIE}}(x, y) \\ &\equiv \frac{r_{\text{cr}}}{2} \frac{\sqrt{f} \lambda(f)}{\sqrt{x^2 + f^2 y^2}}, \end{aligned} \quad (1)$$

where f is the minor-to-major axial ratio of the surface density and is equal to $1 - \epsilon$ (where ϵ is the ellipticity), R_H is the Hubble length c/H_0 , $\hat{D}(z_l, z_s)$ is the angular diameter distance between redshift z_l and z_s ($z_s > z_l$) in units of R_H , and z_l and z_s are respectively the lens and the source redshifts. In equation (1), r_{cr} is the critical radius for the singular isothermal sphere (SIS) (i.e. for $f = 1$) and is given by

$$r_{\text{cr}} = 4\pi \left(\frac{\sigma}{c}\right)^2 R_H \frac{\hat{D}(0, z_l) \hat{D}(z_l, z_s)}{\hat{D}(0, z_s)}, \quad (2)$$

where σ is the line-of-sight velocity dispersion of the galaxy.³ For the case of the SIS, only double imaging is allowed and the cross section for the double imaging is πr_{cr}^2 . For $f \neq 1$, quadruple imaging (and triple imaging for a sufficiently flattened surface density; see below) is possible in addition to double imaging, and the relations between the multiple-imaging cross sections and the line-of-sight velocity dispersion of the galaxy are not unique but depend on the intrinsic shape, the viewing direction, and the distribution function of the galaxy. This dependence is parametrised by $\lambda(f)$ ('dynamical normalisation') in equation (1). In our parametrisation of the SIE in equation (1), $\lambda(f = 1) = 1$ and the case $\lambda(f) = 1$ for any f corresponds to the normalisation in which the mass within the area enclosed by an equidensity ellipse is independent of f (see Kormann, Schneider, & Bartelmann 1994). As shown in Kormann, Schneider, & Bartelmann (1994), for $f < f_0 (\approx 0.3942)$ triple imaging with comparable brightnesses for all three images is possible due to a naked cusp radial caustic. The cross section for the naked-cusp triple-imaging is expected to be small and no case has been found from the CLASS (Browne et al. 2003). Hence we ignore the possibility in the following analyses.

Let $\hat{s}_2(f)$ and $\hat{s}_4(f)$ denote respectively the double imaging and the quadruple imaging cross sections in units of r_{cr}^2 for the case of $\lambda(f) = 1$ for any f . Then, for any given $\lambda(f)$, the double (quadruple) imaging cross section $s_2(f)$ [$s_4(f)$] in units of r_{cr}^2 is given by $s_2(f) = [\lambda(f)]^2 \hat{s}_2(f)$ [$s_4(f) = [\lambda(f)]^2 \hat{s}_4(f)$]. The cross sections for the double imaging and the quadruple imaging for $\lambda(f) = 1$ are respectively given by (Kormann et al. 1994)

$$\begin{aligned} \hat{s}_4(f) &= \frac{4f}{1-f^2} \\ &\times \int_f^1 \left(\frac{\sqrt{1-x^2}}{x} - \arccos x \right) \frac{\sqrt{x^2-f^2}}{x^2} dx, \end{aligned} \quad (3)$$

³ Here we are considering a single-component mass model for the total mass distribution of the galaxy.

and

$$\hat{s}_2(f) = \pi - 2\hat{s}_4(f) \quad (4)$$

which are valid for $f \geq f_0$. Notice that the cross sections given by equations (3) and (4) are for all possible image magnification ratios of the multiple images. However, for the CLASS statistical sample (section 3.1) the observational selection limit on the image magnification ratio for the double imaging is $\mathcal{R} > 0.1$ where \mathcal{R} is the ratio of the flux densities of the fainter to the brighter component. Thus, the double imaging cross section that satisfies the observational limit on the image magnification ratio is less than that given by equation (4) but it can be calculated numerically through a Monte Carlo method. The total cross section for multiple imaging for the SIE is given, in units of r_{cr}^2 , by

$$\begin{aligned} s_{\text{tot}}(f) &= s_2(f) + s_4(f) \\ &= [\lambda(f)]^2 \hat{s}_{\text{tot}}(f) \\ &= [\lambda(f)]^2 [\hat{s}_2(f) + \hat{s}_4(f)]. \end{aligned} \quad (5)$$

The rest of this subsection is devoted to the calculation of the dynamical normalisation factor $\lambda(f)$ in equation (1). For the calculation of the dynamical normalisation, we need to calculate the average of the line-of-sight velocity dispersions for an ensemble of models that are allowed by the axial ratio f of the surface mass density (equation 1). In general, calculations of velocity dispersions of a galaxy require numerically constructing the orbits of the particles in the galaxy that satisfy physical distribution functions $\mathcal{F} \geq 0$.⁴ However, in this paper we consider the cases where the velocity dispersions can be calculated analytically. These are the axisymmetric models, namely the oblate and the prolate spheroid, with distribution functions of the form $\mathcal{F} = \mathcal{F}(E, L_z)$, where E and L_z are respectively the relative energy and the angular momentum component parallel to the symmetry axis. The axisymmetric singular isothermal mass model can be written in the cylindrical coordinates (R, Z) and in the polar coordinates (r, ϑ) by

$$\begin{aligned} \rho &= \rho_0 \frac{1}{R^2 + q^{-2} Z^2} = \frac{\sigma_0^2}{2\pi G} \frac{1}{R^2 + q^{-2} Z^2} \\ &= \frac{\sigma_0^2}{2\pi G} \frac{1}{r^2 (\sin^2 \vartheta + q^{-2} \cos^2 \vartheta)}, \end{aligned} \quad (6)$$

where q is the intrinsic axial ratio of the spheroid. The oblate and the prolate spheroids respectively correspond to $q < 1$ and $q > 1$. For $q = 1$ (i.e. the SIS case), the parameter σ_0 is identical to the one-dimensional velocity dispersion σ (equation 2). Under the assumption that the distribution function has the form $\mathcal{F} = \mathcal{F}(E, L_z)$, the Z -component σ_Z^2 and the R -component σ_R^2 of the second velocity moments are identical [see, e.g., Binney & Tremaine 1987, equation (4-175)]. The azimuthal component of the velocity distribution at a point includes streaming rotation motion as well as random motions. We use the mean squared azimuthal velocity, to be denoted by σ_φ^2 , for our dynamical normalisation calculations since measured line-of-sight velocity dispersions over a large aperture include contributions from any streaming

⁴ In this paper, we use the notation \mathcal{F} for the distribution function, since the notation f is used to denote the surface density axial ratio.

motions. For the axisymmetric scale-free isothermal model given by equation (6), the second velocity moments can be calculated analytically and the expressions include only elementary functions (see, e.g., van der Marel 1994; Qian et al. 1995). The second velocity moments are given for the oblate and the prolate cases as follows: (1) For $q < 1$, we have

$$\begin{aligned}\sigma_R^2(\vartheta) &= \sigma_Z^2(\vartheta) \\ &= \sigma_0^2(1 + q^{-2} \cot^2 \vartheta) \left(\frac{q}{q'}\right)^2 \\ &\quad \times \left[\arctan^2\left(\frac{q'}{q}\right) - \arctan^2\left(\frac{q'}{q} \cos \vartheta\right) \right],\end{aligned}\quad (7)$$

$$\sigma_\phi^2(\vartheta) = 2\sigma_0^2 \frac{q}{q'} \arcsin q' - \sigma_R^2(\vartheta); \quad (8)$$

and (2) for $q > 1$, we have

$$\begin{aligned}\sigma_R^2(\vartheta) &= \sigma_Z^2(\vartheta) \\ &= \frac{\sigma_0^2}{4}(1 + q^{-2} \cot^2 \vartheta) \left(\frac{q}{q'}\right)^2 \\ &\quad \times \left[\ln^2\left(\frac{q+q'}{q-q'}\right) - \ln^2\left(\frac{q+q' \cos \vartheta}{q-q' \cos \vartheta}\right) \right],\end{aligned}\quad (9)$$

$$\sigma_\phi^2(\vartheta) = \sigma_0^2 \frac{q}{q'} \ln\left(\frac{q+q'}{q-q'}\right) - \sigma_R^2(\vartheta). \quad (10)$$

As above, throughout we use the notation $q' \equiv |1 - q^2|^{1/2}$.

We calculate the dynamical normalisations for the oblate and the prolate cases using the above equations (7), (8), (9) and (10).

a. The oblate case ($q < 1$)—The radial component σ_R^2 and the azimuthal component σ_ϕ^2 of the second velocity moments in the cylindrical coordinates can be used to obtain a Cartesian component σ_X^2 that is perpendicular to the symmetry axis, namely we have

$$\sigma_X^2 = \sigma_R^2 \cos^2 \varphi + \sigma_\phi^2 \sin^2 \varphi. \quad (11)$$

The mass-weighted average of a second velocity moment is defined by

$$\overline{\sigma^2} \equiv \frac{1}{\int \rho(r^2 \sin \vartheta dr d\vartheta d\varphi)} \int \rho \sigma^2(r^2 \sin \vartheta dr d\vartheta d\varphi). \quad (12)$$

Using the above definition (equation 12), we obtain for the mass-weighted averages of the X and the Z components respectively in units of σ_0^2

$$W_X^{\text{obl}}(q) \equiv \overline{\sigma_X^2} / \sigma_0^2 = \frac{q}{q'} \arcsin q', \quad (13)$$

and

$$\begin{aligned}W_Z^{\text{obl}}(q) &\equiv \overline{\sigma_Z^2} / \sigma_0^2 \\ &= \frac{1}{2} \frac{q}{q'} \left(\arctan \frac{q'}{q} \right)^{-1} \int_0^\pi d\vartheta \frac{1}{\sin \vartheta} \\ &\quad \times \left(\arctan^2 \frac{q'}{q} - \arctan^2 \frac{q' \cos \vartheta}{q} \right).\end{aligned}\quad (14)$$

Given the mass-weighted averages of the two Cartesian components, the line-of-sight component of the second velocity moments when the galaxy is viewed at an inclination angle of i , with $i = \pi/2$ defining the edge-on view, is given by

$$\sigma_{\text{los}}^2(i) = \sigma_0^2 [W_Z^{\text{obl}}(q) \cos^2 i + W_X^{\text{obl}}(q) \sin^2 i]. \quad (15)$$

For a given axial ratio f of the projected surface density given by equation (1), there are infinitely many combinations of inclination angle i and intrinsic axial ratio q that are consistent with the projected axial ratio f . Averaging equation (15) over this ensemble of models, we have

$$\langle \sigma_{\text{los}}^2 \rangle = (\pi/2 - i_{\text{min}})^{-1} \int_{i_{\text{min}}}^{\pi/2} \sigma_{\text{los}}^2(i) di, \quad (16)$$

where i_{min} is the minimum possible inclination angle for the given projected axial ratio f . From the relation

$$f^2 = \cos^2 i + q^2 \sin^2 i = 1 - q'^2 \sin^2 i \quad (17)$$

(for $q < 1$), we have

$$i_{\text{min}} = \arcsin f', \quad (18)$$

where and throughout we use the notation $f' \equiv (1 - f^2)^{1/2}$. Introducing the variable $t = \sin i$, we can write the inclination-averaged line-of-sight velocity second moment as

$$\begin{aligned}\langle \sigma_{\text{los}}^2 \rangle(f') &= \sigma_0^2 (\pi/2 - \arcsin f')^{-1} \\ &\quad \times \int_{f'}^1 \{ [W_X^{\text{obl}}(q(t)) - W_Z^{\text{obl}}(q(t))] t^2 \\ &\quad + W_Z^{\text{obl}}(q(t)) \} \frac{dt}{\sqrt{1-t^2}}.\end{aligned}\quad (19)$$

The projected surface density for the oblate case of the axisymmetric mass distribution given by equation (6) can be written as

$$\Sigma^{\text{obl}} = \frac{\sigma_0^2}{2G} q \frac{1}{\sqrt{x^2 + f^2 y^2}} \Rightarrow \Sigma^{\text{obl}} = \frac{\sigma_0^2}{2G} \langle q \rangle \frac{1}{\sqrt{x^2 + f^2 y^2}}, \quad (20)$$

where $\langle q \rangle$ is the inclination averaged value of the axial ratio, which can be shown to be

$$\langle q \rangle = \langle q \rangle(f) = (\pi/2 - \arcsin f')^{-1} \frac{\pi}{4} f^2 F\left(1, \frac{1}{2}; 2; f^2\right), \quad (21)$$

where F is a hypergeometric function. Finally, comparing equation (20) with equation (1) in conjunction with the relations given by equations (19) and (21), we obtain for the dynamical normalisation of the singular isothermal oblate spheroid with a distribution function of the form $F = F(E, L_z)$

$$\begin{aligned}\lambda^{\text{obl}}(f) &= \frac{\pi}{4} f^{3/2} F\left(1, \frac{1}{2}; 2; f^2\right) \\ &\quad \times \left[\int_{f'}^1 \{ [W_X^{\text{obl}}(q(t)) - W_Z^{\text{obl}}(q(t))] t^2 \right. \\ &\quad \left. + W_Z^{\text{obl}}(q(t)) \} \frac{dt}{\sqrt{1-t^2}} \right]^{-1}.\end{aligned}\quad (22)$$

b. The prolate case ($q > 1$)—A procedure similar to the above procedure for the oblate case can be followed using equations (9) and (10) to obtain the dynamical normalisation for the prolate spheroid. We point out the differences in the procedures between the oblate and the prolate cases and then list the calculated results. First, the projected axial ratio $f (< 1)$ is related to the intrinsic axial ratio $q (> 1)$ via

$$f^2 = (\cos^2 i + q^2 \sin^2 i)^{-1} = (1 + q'^2 \sin^2 i)^{-1}. \quad (23)$$

Second, the projected surface density for the prolate case of the axisymmetric mass distribution given by equation (6)

can be written using equation (23) as

$$\begin{aligned}\Sigma^{\text{prol}} &= \frac{\sigma_0^2}{2G} f q \frac{1}{\sqrt{x^2 + f^2 y^2}} \Rightarrow \\ \Sigma^{\text{prol}} &= \frac{\sigma_0^2}{2G} f \langle q \rangle \frac{1}{\sqrt{x^2 + f^2 y^2}}.\end{aligned}\quad (24)$$

Finally, the requirement of the positivity of the second velocity moments shows that the intrinsic axial ratio q cannot be greater than $q_{\text{max}} = 3.46717\dots$ and thus the minimum inclination angle i_{min} for the given projected axial ratio f is given by

$$i_{\text{min}} = \arcsin t_{\text{min}} = \arcsin \left(\frac{1}{\sqrt{q_{\text{max}}^2 - 1}} \frac{f'}{f} \right).\quad (25)$$

Unfortunately, even for $q < q_{\text{max}}$, non-negativity of the distribution function is not guaranteed. In other words, our adopted (simple-minded) dynamical model for the singular isothermal prolate spheroid has an unphysical feature. Nonetheless, our adopted dynamical model was sometimes used in the literature as a simple approximation. Furthermore, the construction of a physical dynamical model in conjunction with a prolate mass model that would mimic the SIE is beyond the scope of this paper. Bearing the above in mind, we now give the calculated results. The dynamical normalisation of the singular isothermal prolate spheroid with a distribution function of the form $\mathcal{F} = \mathcal{F}(E, L_z)$ is given by

$$\begin{aligned}\lambda^{\text{prol}}(f) &= \left(\int_{t_{\text{min}}}^1 \sqrt{\frac{t^2 f^2 + f'^2}{f(1-t^2)}} \frac{dt}{t} \right) \\ &\times \left[\int_{t_{\text{min}}}^1 \{ [W_X^{\text{prol}}(q(t)) - W_Z^{\text{prol}}(q(t))] t^2 \right. \\ &\quad \left. + W_Z^{\text{prol}}(q(t)) \} \frac{dt}{\sqrt{1-t^2}} \right]^{-1}.\end{aligned}\quad (26)$$

where

$$W_X^{\text{prol}}(q) = \frac{1}{2} \frac{q}{q'} \ln \frac{q+q'}{q-q'},\quad (27)$$

and

$$\begin{aligned}W_Z^{\text{prol}}(q) &= \frac{1}{4} \frac{q}{q'} \left(\ln \frac{q+q'}{q-q'} \right)^{-1} \int_0^\pi d\vartheta \frac{1}{\sin \vartheta} \\ &\times \left[\left(\ln \frac{q+q'}{q-q'} \right)^2 - \left(\ln \frac{q+q' \cos \vartheta}{q-q' \cos \vartheta} \right)^2 \right]\end{aligned}\quad (28)$$

Fig. 1 shows the functional behaviour of the dynamical normalisation squared for the following three cases; $\lambda(f) = \lambda^{\text{obl}}(f)$, $\lambda(f) = 0.5\lambda^{\text{obl}}(f) + 0.5\lambda^{\text{prol}}(f)$, and $\lambda(f) = \lambda^{\text{prol}}(f)$, where $\lambda^{\text{obl}}(f)$ and $\lambda^{\text{prol}}(f)$ are respectively given by equations (22) and (26) (see section 2.1.1).

2.1.2 Galaxy luminosity functions, magnification biases, and lensing probabilities

We assume that galaxies of a given morphological type are uniformly distributed in comoving space and distributed in luminosity following a Schechter (1976) luminosity function and that the luminosity of a galaxy has a power-law relation

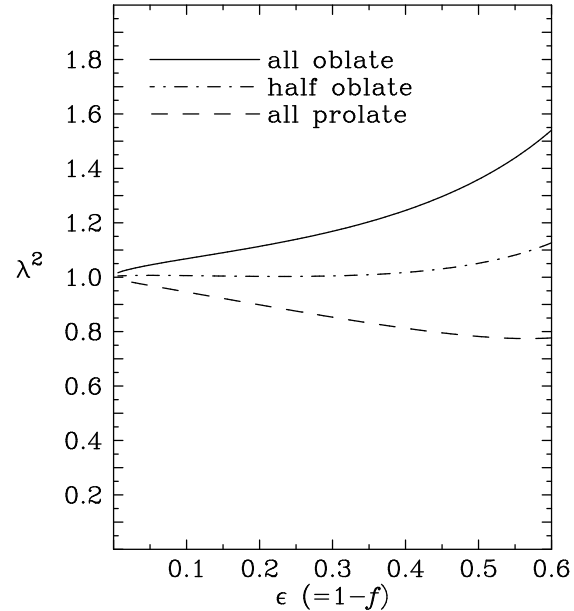


Figure 1. Functional behaviour of the lens ‘dynamical normalisation’ squared. We consider three cases of the dynamical normalisation, namely $\lambda(f) = \lambda^{\text{obl}}(f)$, $\lambda(f) = 0.5\lambda^{\text{obl}}(f) + 0.5\lambda^{\text{prol}}(f)$, and $\lambda(f) = \lambda^{\text{prol}}(f)$, where $\lambda^{\text{obl}}(f)$ and $\lambda^{\text{prol}}(f)$ are respectively the dynamical normalisations for the oblate and the prolate scale-free isothermal spheroids.

to its line-of-sight velocity dispersion (i.e. the Faber-Jackson relation for early-type galaxies and the Tully-Fisher relation for late-type galaxies). The differential probability for a source with redshift z_s and flux density S_ν to be multiply-imaged with image multiplicity m and image separation $\Delta\theta$ to $\Delta\theta + d(\Delta\theta)$, due to a distribution of intervening galaxies of morphological type g (where $g = e$ for early-type galaxies and s for late-type galaxies) at redshifts z to $z + dz$ modelled by SIEs and described by a Schechter luminosity function, is given by

$$\begin{aligned}\frac{d^2 p_m^{(g)}(z, \Delta\theta; z_s, S_\nu)}{dz d(\Delta\theta)} &= s_m(f) 8\pi^2 \gamma R_H^3 \\ &\times n_*(z) (1+z)^3 \left[\frac{\sigma_*(z)}{c} \right]^4 \\ &\times \left| \frac{d\ell}{dz} \right| \left[\frac{\hat{D}(0, z) \hat{D}(z, z_s)}{\hat{D}(0, z_s)} \right]^2 \\ &\times \frac{1}{\Delta\theta_*(z)} \left[\frac{\Delta\theta}{\Delta\theta_*(z)} \right]^{(\alpha\gamma + \gamma + 2)/2} \\ &\times \exp \left[- \left(\frac{\Delta\theta}{\Delta\theta_*(z)} \right)^{\gamma/2} \right] \\ &\times B_m(z_s, S_\nu),\end{aligned}\quad (29)$$

where $s_m(f)$ (hereafter, $m = 2, 4$) is the cross section in units of r_{cr}^2 (equation 2) for multiple imaging with image multiplicity m (section 2.1.1), $\Delta\theta_*(z)$ is the characteristic image separation (see below), and $B_m(z_s, S_\nu)$ is the magnification bias (see below). In equation (29), $|d\ell/dz|$, where

$\ell = H_0 \times (\text{proper time})$, is given by

$$\left| \frac{d\ell}{dz} \right| = (1+z)^{-1} [\Omega_m (1+z)^3 + (1 - \Omega_m - \Omega_\Lambda)(1+z)^2 + \Omega_\Lambda]^{-1/2} \quad (30)$$

for a cosmology with a classical cosmological constant. In equation (29), we have also used the following notations: the Schechter (1976) function

$$\frac{dn(L, z)}{dL} = \frac{n_*(z)}{L_*(z)} \left[\frac{L}{L_*(z)} \right]^\alpha \exp[-L/L_*(z)], \quad (31)$$

where α is the faint-end slope, $L_*(z)$ is the characteristic luminosity, and $n_*(z)$ is the characteristic comoving number density which can be written as

$$n_*(z) = n_{*,0} e_n(z). \quad (32)$$

The luminosity of a galaxy is assumed to be correlated with its line-of-sight velocity dispersion by

$$\frac{L}{L_*(z)} = 10^{0.4[M_*(z) - M]} = \left[\frac{\sigma}{\sigma_*(z)} \right]^\gamma \quad (33)$$

where $M_*(z)$ and $\sigma_*(z)$ are respectively the characteristic absolute magnitude and the characteristic velocity dispersion corresponding to the characteristic luminosity $L_*(z)$, and γ is the Faber-Jackson or Tully-Fisher exponent. We write the characteristic velocity dispersion as

$$\sigma_*(z) = \sigma_{*,0} e_v(z). \quad (34)$$

In equation (29), the characteristic image separation $\Delta\theta_*(z)$ by an L_* galaxy is given by

$$\Delta\theta_*(z) = \lambda(f) 8\pi \frac{\hat{D}(z, z_s)}{\hat{D}(0, z_s)} \left[\frac{\sigma_*(z)}{c} \right]^2, \quad (35)$$

where $\lambda(f)$ is the dynamical normalisation. Notice that the characteristic image separation $\Delta\theta_*(z)$ (equation 35) scales linearly with the dynamical normalisation $\lambda(f)$, while the multiple imaging cross sections $s_m(f)$ scale quadratically with $\lambda(f)$ (section 2.1.1). In equations (32) and (34), parameters $e_n(z)$ and $e_v(z)$ respectively represent the evolutions of the number density and the velocity dispersion of galaxies.

The magnification bias $B_m(z_s, S_\nu)$ in equation (29), namely the factor by which the multiply-imaged sources are overrepresented compared with the unlensed sources in a flux limited sample because the multiply-imaged sources come from intrinsically fainter populations compared with the unlensed ones of the same apparent brightness (see, e.g., Maoz & Rix 1993; King & Browne 1996), is given by

$$B_m(z_s, S_\nu) = \left[\int_{\mu_{m,\min}}^{\mu_{m,\max}} \left| \frac{dN_{z_s}(> S_\nu/\mu_m)}{dS_\nu} \frac{dP_m(> \mu_m)}{d\mu_m} \right| \times \frac{1}{\mu_m} d\mu_m \right] \left| \frac{dN_{z_s}(> S_\nu)}{dS_\nu} \right|^{-1} \quad (36)$$

($m = 2, 4$). Here $N_{z_s}(> S_\nu)$ is the intrinsic number-flux density relation, i.e. the integrated source counts as a function of flux density S_ν , for the source population at redshift z_s . Parameter μ_m denotes the total magnification for multiple imaging with image multiplicity m , namely the sum of the absolute magnifications of the m images. $P_m(> \mu_m)$ is the fraction of the multiple imaging cross

section with image multiplicity m that have total magnifications greater than μ_m , for a given lens model. Hence $|dP_m(> \mu_m)/d\mu_m|$ is the magnification probability distribution above a minimum possible magnification $\mu_{m,\min}$ and it follows that $P_m(> \mu_{m,\min}) = 1$. For example, for the SIS the magnification probability distribution for double imaging with any magnification ratio of the two images is given by $|dP_2^{\text{SIS}}(> \mu_2)/d\mu_2| = 8/\mu_2^3$ with the minimum total magnification of $\mu_{2,\min} = 2$. The minimum and maximum total magnifications $\mu_{m,\min}$ and $\mu_{m,\max}$ in equation (36) depend on observation characteristics as well as the lens model. For multiple imaging of a point source, $\mu_{m,\max} \rightarrow \infty$. For the CLASS statistical sample, the observational lower limit on the ratio of the flux densities of the fainter to the brighter image for the doubly-imaged systems is $\mathcal{R}_{\min} = 0.1$. Given such an observational limit \mathcal{R}_{\min} , the minimum total magnification for double imaging for the SIS model is given by

$$\mu_{2,\min}^{\text{SIS}} = 2 \frac{1 + \mathcal{R}_{\min}}{1 - \mathcal{R}_{\min}}. \quad (37)$$

For the SIE (i.e. $f \neq 1$ in equation 1), we numerically calculate magnification probability distributions and minimum total magnifications. We do this by solving the simplified lens equation for the SIE (Kormann et al. 1994) for millions of source positions randomly distributed on a source region that includes the region enclosed by the caustics for each value of the axis ratio f . Fig. 2(a) shows several examples of the magnification probability distribution $|dP_m(> \mu_m)/d\mu_m|$ for double and quadruple imaging. Fig. 2(b) shows the theoretical minimum total magnifications for double and quadruple imaging, i.e. for any magnification ratios, and the minimum total magnifications for double imaging with the CLASS observational limit $\mathcal{R} > 0.1$.

The differential probability for a source to be multiply-imaged with image multiplicity m and image separation $\Delta\theta$ to $\Delta\theta + d(\Delta\theta)$ due to all the galaxies of type g from $z = 0$ to z_s , can be obtained from equation (29):

$$\frac{dp_m^{(g)}(\Delta\theta; z_s, S_\nu)}{d(\Delta\theta)} = \int_0^{z_s} \frac{d^2 p_m^{(g)}(z, \Delta\theta; z_s, S_\nu)}{dz d(\Delta\theta)} dz. \quad (38)$$

Likewise, the differential probability for a source to be multiply-imaged with image multiplicity m and with any image separation $\geq \Delta\theta_{\min}$ ⁵ due to galaxies of type g at redshifts z to $z + dz$ is given by

$$\begin{aligned} \frac{dp_m^{(g)}(z; z_s, S_\nu)}{dz} &= s_m(f) 16\pi^2 \Gamma \left(\alpha + 1 + \frac{4}{\gamma} \right) R_H^3 \\ &\times n_*(z) (1+z)^3 \left[\frac{\sigma_*(z)}{c} \right]^4 \\ &\times \left| \frac{d\ell}{dz} \right| \left[\frac{\hat{D}(0, z) \hat{D}(z, z_s)}{\hat{D}(0, z_s)} \right]^2 \\ &\times B_m(z_s, S_\nu) \\ &- \int_0^{\Delta\theta_{\min}} \frac{d^2 p_m^{(g)}(z, \Delta\theta; z_s, S_\nu)}{dz d(\Delta\theta)} d(\Delta\theta), \end{aligned} \quad (39)$$

⁵ An upper limit on $\Delta\theta$ is not necessary since the lensing probability due to galaxy lenses (given by equation 29) is negligibly small beyond an observational limit, e.g. several arcseconds.

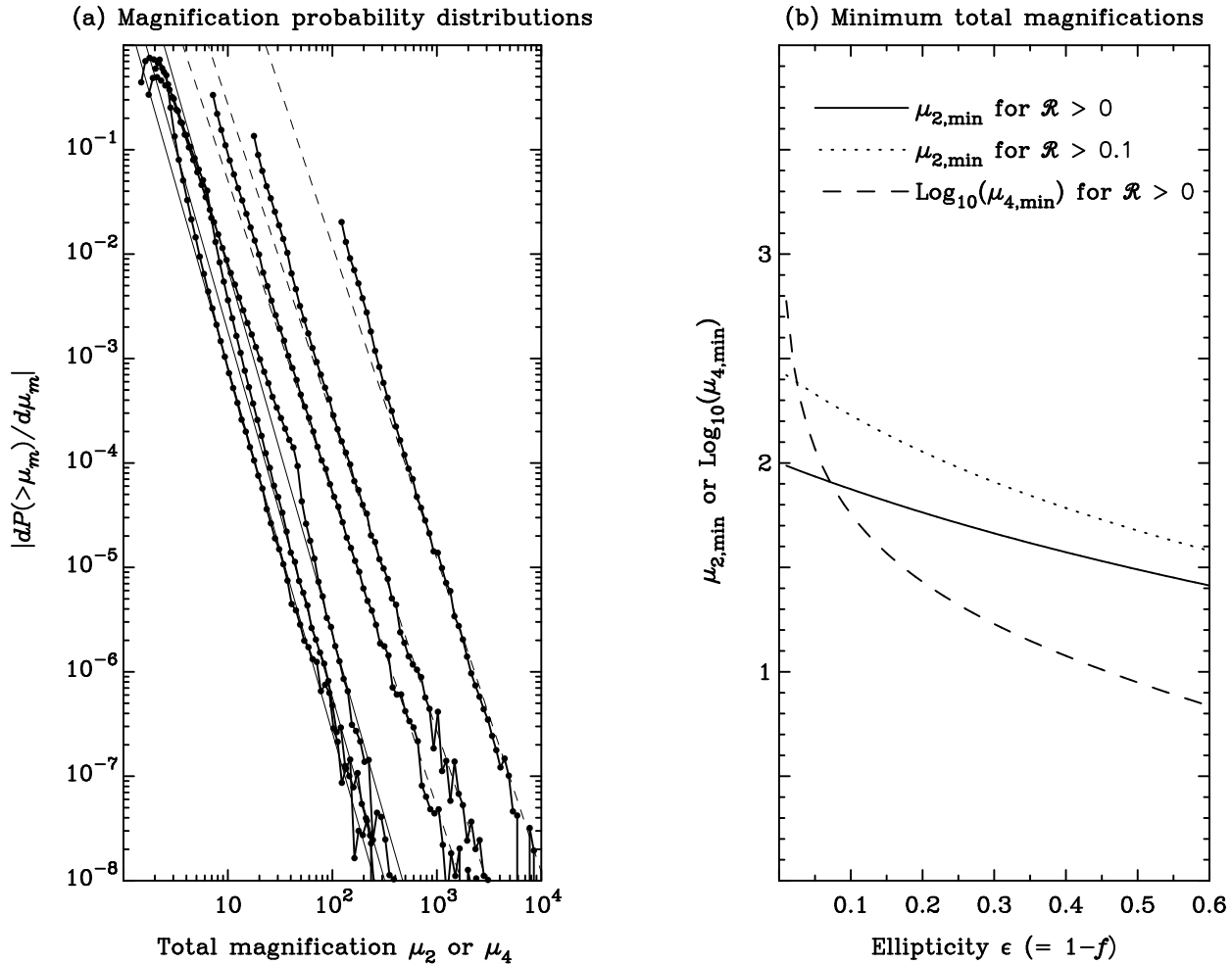


Figure 2. (a) Magnification probability distributions (MPDs). The six curves from right to left respectively correspond to MPDs for quadruple imaging by $\epsilon = 0.05, 0.3$ and 0.6 SIEs and for double imaging by $\epsilon = 0.05, 0.3$ and 0.6 SIEs. The thin solid lines representing $\mu_2^{-7/2}$ behaviours and the thin dashed lines representing μ_4^{-3} behaviours fit respectively well the numerical data points for double imaging and quadruple imaging at high magnifications in agreement with the expectations from analytical calculations. (b) Minimum total magnifications for double and quadruple imaging by SIEs as a function of ellipticity ϵ . The solid line shows the minimum total magnifications for double imaging for any magnification ratios between the two images. The dotted line shows the minimum total magnifications for double imaging only for the fainter image to the brighter image magnification ratio $\mathcal{R} > 0.1$, which is the observational limit for the final CLASS statistical sample. The dashed line shows the minimum total magnifications for quadruple imaging for any magnification ratios between the four images.

where the integrand in the last piece of the right-hand side is given by equation (29). Finally, using equation (39) we obtain the integrated probability for the multiple imaging with image multiplicity m due to galaxies of type g :

$$p_m^{(g)}(z_s, S_\nu) = \int_0^{z_s} \frac{dp_m^{(g)}(z; z_s, S_\nu)}{dz} dz. \quad (40)$$

2.1.3 Summary of model parameters

The lensing probabilities given by equations (29), (38), (39) and (40) are for a population of galaxies of a specific morphological type that are assumed to be described by a set of Schechter parameters n_* , α , and M_* with corresponding L_* and σ_* along with the Faber-Jackson or Tully-Fischer exponent γ (equation 33). We assume two populations of galaxies separately contributing to multiple imaging, namely the

early-type (i.e. ellipticals and S0s) and the late-type (i.e. spirals and other non-E/S0s) populations. Separately taking into account the two populations is required. This is because the early-type and the late-type galaxies are dynamically different, satisfy respectively the Faber-Jackson and the Tully-Fisher relations, and have different characteristics in multiple imaging: the multiple imaging rate by the early-type population is $\approx 3-6$ times higher and the early-type galaxies produce on average larger image splittings.

The parameters of our statistical lensing model can be summarized as follows: (1) up to three cosmological parameters: \bullet matter density Ω_m , \bullet density of a classical cosmological constant Ω_Λ or dark energy density Ω_x with \bullet its constant equation of state $w = p_x(\text{pressure})/\rho_x(\text{energy den-}$

sity);⁶ (2) six parameters for the early-type galaxy population, i.e. early-type Schechter parameters $n_{*,0}^{(e)}$, $\sigma_*^{(e)}$, and $\alpha^{(e)}$, Faber-Jackson exponent γ_{FJ} , early-type mean mass ellipticity $\bar{\epsilon}^{(e)}$, and relative frequency of the oblatenesses $\mathcal{P}_{\text{obl}}^{(e)}$ among early-type galaxies; (3) six parameters for the late-type galaxy population, i.e. late-type Schechter parameters $n_{*,0}^{(s)}$, $\sigma_*^{(s)}$, and $\alpha^{(s)}$, Tully-Fisher exponent γ_{TF} , late-type mean mass ellipticity $\bar{\epsilon}^{(s)}$, and relative frequency of the oblatenesses $\mathcal{P}_{\text{obl}}^{(s)}$ among late-type galaxy halos.⁷

In addition to the above parameters, our statistical lensing model includes the parameters that can be used to model certain aspects of galaxy evolutions, i.e., $e_n^{(g)}(z)$ and $e_v^{(g)}(z)$ where $g = e, s$ (see equations 32 and 34). In this work, we assume no evolution of the comoving number densities of galaxies for the redshift range which is relevant to lensing by CLASS sources, i.e., $e_n^{(g)}(z) = 1$ for $0 \leq z \lesssim 1$. Here note that any significant evolution of the comoving number density of late-type galaxies has little effect on the derived values of cosmological parameters. Note also that while a significant evolution of the comoving number density of early-type galaxies would have a significant effect on the derived values of cosmological parameters, (our interpretation of) current observational evidence suggests that there has been little evolution of the comoving number density of early-type galaxies since $z \sim 1$ (see the last paragraph of section 3.3). However, evolution of the comoving number density of early-type galaxies is a main source of uncertainty and its systematic effects on the derived values of cosmological parameters are discussed in section 5.3.3. Since the characteristic velocity dispersions will be treated as free parameters (section 4) and lens redshifts are intermediate, it should be understood that parameters $e_v^{(g)}(z)$ are irrelevant and we are constraining parameters $\sigma_*^{(g)}$ for $0.3 \lesssim z \lesssim 1$. Finally, in addition to the cosmological parameters and the lens parameters, there are parameters used to describe the CLASS source population, namely the redshift distribution and the number–flux-density relation, which can be found in section 3.2.

2.2 Method of statistical analysis

For a statistical sample that contains N_{L} multiply-imaged sources and N_{U} unlensed sources, the likelihood \mathcal{L} of the observation data given the statistical lensing model is defined by

$$\ln \mathcal{L} = \sum_{k=1}^{N_{\text{U}}} \ln \left[1 - \sum_{m=2,4} p_m^{(\text{all})}(z_{s,k}, S_{\nu,k}) \right]$$

⁶ Here all the cosmological densities refer to the fractions of the present critical density.

⁷ In this work, we are considering a single-component galaxy model. This means that for a spiral galaxy the mass model is intended to approximate the total mass distribution by the halo, the bulge and the disk of the galaxy. Consequently, the model parameters (i.e., velocity dispersion and projected ellipticity) are effective quantities corresponding to the combined lensing effects by the components of the galaxy. Discussions on the lensing effects by the components of a spiral galaxy can be found, e.g., in Keeton & Kochanek (1998).

$$+ \sum_{l=1}^{N_{\text{L}}} \ln \delta p_{m_l}^{(\text{one})}[(z_l), \Delta\theta_l; z_{s,l}, S_{\nu,l}], \quad (41)$$

where $\sum_{m=2,4} p_m^{(\text{all})}(z_{s,k}, S_{\nu,k})$ is the sum of the double and quadruple imaging probabilities (equation 40) for the k -th unlensed source, and $\delta p_{m_l}^{(\text{one})}[(z_l), \Delta\theta_l; z_{s,l}, S_{\nu,l}]$ is the differential probability (equation 29, 38, or 39) for the l -th multiply-imaged source, which is a specific probability including the observed configuration of the source, i.e. its image separation $\Delta\theta_l$, its image multiplicity m_l (and its lens redshift z_l if it is known).

In equation (41), for the unlensed sources the probability to be used is the sum of the probabilities due to the early-type and the late-type populations, namely

$$p_m^{(\text{all})}(z_{s,k}, S_{\nu,k}) \equiv p_m^{(e)}(z_{s,k}, S_{\nu,k}) + p_m^{(s)}(z_{s,k}, S_{\nu,k}), \quad k = 1, 2, \dots, N_{\text{U}}. \quad (42)$$

For the multiply-imaged sources, the suitable differential probability can be given by

$$\begin{aligned} \delta p_{m_l}^{(\text{one})}[(z_l), \Delta\theta_l; z_{s,l}, S_{\nu,l}] &\equiv \\ &\omega_l^{(e)} \delta p_{m_l}^{(e)}[(z_l), \Delta\theta_l; z_{s,l}, S_{\nu,l}] \\ &+ \omega_l^{(s)} \delta p_{m_l}^{(s)}[(z_l), \Delta\theta_l; z_{s,l}, S_{\nu,l}], \\ &l = 1, 2, \dots, N_{\text{L}}, \end{aligned} \quad (43)$$

where parameters $\omega_l^{(e)}$ and $\omega_l^{(s)}$ are the weights given to the early-type and the late-type populations, respectively, satisfying $\omega_l^{(e)} + \omega_l^{(s)} = 1$. If the lensing galaxy type is known to be an early-type (late-type), $\omega_l^{(e)} = 1$ ($\omega_l^{(s)} = 1$). If the lensing galaxy type is unknown, we use $\omega_l^{(g)} = \delta p_{m_l}^{(g)} / [\delta p_{m_l}^{(e)} + \delta p_{m_l}^{(s)}]$ ($g = e, s$), if the lens redshift is known, whereas we use $\omega_l^{(e)} = 0.8$ and $\omega_l^{(s)} = 0.2$ otherwise.

From equation (41), a “ χ^2 ” is defined by

$$\chi^2 = -2 \ln \mathcal{L} \quad [+ \text{Gaussian prior on } \sigma_*^{(s)}]. \quad (44)$$

As indicated in the bracket in equation (44), the χ^2 will sometimes include a Gaussian prior probability term of the late-type characteristic velocity dispersion $\sigma_*^{(s)}$. We determine ‘best-fit’ model parameters by minimizing the χ^2 (equation 44) and obtain confidence limits on the model parameters using the usual $\Delta\chi^2$ ($\equiv \chi^2 - \chi_{\text{min}}^2$)-static, where χ_{min}^2 is the global minimum χ^2 for the best-fit parameters.

3 INPUT DATA

In this section, we summarize data both from CLASS observations and recent large-scale observations of galaxies that will be used as the input for the statistical lensing model described in section 2. In section 3.1, we briefly review the definition of the final CLASS statistical sample that satisfy well-defined observational selection criteria (Browne et al. 2003) and summarize the properties of the multiply-imaged sources in the sample. In section 3.2, we summarize observational information on flat-spectrum radio sources including that from CLASS observations and estimate the distribution of CLASS radio sources in redshift and flux density. In section 3.3, we survey recent observational results for galaxy luminosity functions and obtain estimates of galaxy lumi-

nosity functions per morphological type based on the data from the literature.

3.1 The final CLASS statistical sample

The Cosmic Lens All-Sky Survey is the largest completed (radio-selected) galactic mass scale gravitational lens search project. The CLASS project along with its predecessor project the Jodrell-Bank–VLA Astrometric Survey (JVAS; see, e.g., King et al. 1999) identified 22 multiply-imaged systems out of a total of 16521 radio sources targeted (Myers et al. 2003; Browne et al. 2003). Out of the entire CLASS sample including the JVAS sources, a subsample of 8958 sources containing 13 multiply-imaged systems constitutes a statistical sample that satisfies well-defined observational selection criteria (Browne et al. 2003). The final CLASS statistical sample is the largest sample that can be used for the purpose of statistical analyses of gravitational lensing. The reader is referred to Myers et al. (2003) and Browne et al. (2003) for the description of the CLASS observations including the selection of the targets, the gravitational lens candidate selection process, the follow-up observations of the lens candidate sources, and the properties of the finally confirmed individual multiply-imaged systems. From Browne et al. (2003), the final CLASS statistical sample satisfies the following well-defined selection criteria that are observationally reliable:

- (i) The spectral index between 1.4 GHz and 5 GHz is flatter than -0.5 , i.e. $\alpha \geq -0.5$ with $S_\nu \propto \nu^\alpha$.
- (ii) The total flux density of (the components of) each source ≥ 30 mJy at 5 GHz.
- (iii) The total flux density of (the components of) each source ≥ 20 mJy at 8.4 GHz.
- (iv) For multiply-imaged systems, (a) the compact radio-core images have separations ≥ 300 milli-arcseconds, and (b) for doubly-imaged systems the ratio of the flux densities of the fainter to the brighter images is ≥ 0.1 .

The final CLASS statistical sample includes JVAS sources which essentially form the bright tail with their flux densities ≥ 200 mJy at 5 GHz. However, not all JVAS sources are included in the final CLASS statistical sample because of the strict application of the above criteria (i) and (iv).

The properties of the 13 multiply-imaged systems contained in the final CLASS statistical sample are summarized in Table 1. Notice that two out of the four multiply-imaged sources in the JVAS (statistical) sample used by Helbig et al. (1999), namely 0414+054 and 1030+074, are excluded because 0414+054 has too steep a spectral index and 1030+074 has two images whose fainter-to-brighter image flux-density ratio is less than 0.1. Notice also that JVAS system 2114+022 which was excluded by Helbig et al. (1999) is included along with other multiple-galaxy lens systems. The total flux densities, the lens redshifts (if measured), the source redshifts (see below for sources without measured redshifts), the image separations, the image multiplicities, and the lensing galaxy types (if determined), as given in Table 1, are all used (through the likelihood function defined in section 2.2) to constrain the parameters of the statistical lensing model. However, the measured image separations of 1359+154, 1608+656, and 2114+022 are not

used because the observed angular sizes are due to multiple galaxies within their critical radii and thus should not be used to constrain parameters pertaining to single galaxies. Notice particularly that lens modelling of these systems shows that the inferred critical radii of the secondary (and tertiary) galaxies are comparable in size to those of the corresponding primary galaxies; the ratio of the smallest to the largest critical radii ranges from 66% to 81% assuming singular isothermal mass models for individual galaxies [see Rusin et al. (2001a) for 1349+154, Koopmans & Fassnacht (1999) for 1608+656, and Chae, Mao, & Augusto (2001) for 2114+022]. Furthermore, the inferred critical radii of the primary galaxies for the multiple-galaxy lens systems are similar to those of the early-type lensing galaxies for the single-galaxy lens systems for which no comparably massive secondary galaxies are observed or required for lens modelling; specifically, the average critical radius of the primary galaxies for 1349+154, 1608+656, and 2114+022 is 1.34 arcsec while that for eight (presumably) early-type single-galaxy lens systems, namely 0445+123, 0631+519, 0712+472, 0850+054, 1152+199, 1422+231, 1933+503, and 2319+051 (see below why 2045+265 is excluded), is 1.23 arcsec. These results suggest that discarding the observed image separations for the multiple-lens systems 1349+154, 1608+656, and 2114+022 would be an appropriate way of interpreting the data. Likewise, the image multiplicities of the above three systems are not used to constrain mean mass ellipticity of galaxies because asymmetries in the total potentials of these systems are caused by combinations of multiple potentials. The image separation of 2045+265 is not used because of present uncertainties in the details of the lensing scenario. For the multiply-imaged sources without measured source redshifts, we take $z_s = 2$ which is the mean source redshift for the multiply-imaged sources with measured source redshifts.

3.2 Global properties of flat-spectrum radio sources

As seen in section 2.1.2, the calculation of the lensing probability (equations 29, 38, 39, or 40) for a source requires the knowledge of the differential number–flux-density relation ($|dN_{z_s}(> S_\nu)/dS_\nu|$) that the source follows and the redshift of the source (z_s). More specifically, the differential number–flux-density relation is required in the calculation of the magnification bias (equation 36). In particular, the differential number–flux-density relation needs to be known from the flux density of the source to lower flux densities (formally to the zero flux density). Furthermore, the differential number–flux-density relation needs to be known as a function of source redshift. However, systematic measurements have been done only for a few dozens of CLASS sources (Marlow et al. 2000). For this reason, we are led to ignore any redshift dependence of the differential number–flux-density relation. We also ignore weak dependences of the differential number–flux-density relation on the spectral index of the source for the sake of simplicity.

The final CLASS statistical sample is well-described at $\nu = 5$ GHz by $|dN(> S_5)/dS_5| \propto (S_5/S_5^0)^{-\eta}$ with $\eta = 2.07 \pm 0.02$ for $S_5^0 < S_5 \lesssim 1$ Jy where $S_5^0 = 30$ mJy (McKean et al., in preparation). For flux densities lower than S_5^0 , McKean et al. (in preparation) find $\eta = 1.97 \pm 0.14$

Table 1. Multiply-imaged systems in the final CLASS statistical sample. The ratio of the flux densities of the images is given for the doubles only. Probable lens galaxy morphological-type identification is given using the codes, ‘e’ for an early-type and ‘s’ for a spiral. The references for the morphological type identifications are: (1) Browne et al. (1993); (2) Fassnacht & Cohen (1998); (3) Impey et al. (1996); (4) Myers et al. (1995); (5) Sykes et al. (1998); (6) Augusto et al. (2001); (7) Rusin et al. (2001b).

Source	Survey	Total flux density (mJy)	Source redshift z_s	Lens redshift z_l	Maximum image separation (arcsec)	Image flux-density ratio	Number of images	Lensing galaxy type
0218+357	JVAS	1480.	0.96	0.68	0.334	0.26	2	s ¹
0445+123	CLASS	50.	-	-	1.33	0.14	2	-
0631+519	CLASS	88.	-	-	1.16	0.15	2	-
0712+472	CLASS	30.	1.34	0.41	1.27	-	4	e ²
0850+054	CLASS	68.	-	-	0.68	0.14	2	-
1152+199	CLASS	76.	1.019	0.439	1.56	0.33	2	-
1359+154	CLASS	66.	3.235	-	1.65	-	6	-(3 Gs)
1422+231	JVAS	548.	3.62	0.34	1.28	-	4	e ³
1608+656	CLASS	88.	1.39	0.64	2.08	-	4	e (2 Gs) ⁴
1933+503	CLASS	63.	2.62	0.755	1.17	-	4	e ^{5?}
2045+265	CLASS	55.	-	0.867	1.86	-	4	-
2114+022	JVAS	224.	-	0.32/0.59	2.57	0.33	2?	e (2 Gs) ⁶
2319+051	CLASS	76.	-	0.624/0.588	1.36	0.18	2	e ⁷

based on a Very Large Array (VLA) mapping of selected regions of the sky down to $S_5 = 5$ mJy. The differential number–flux-density relation can also be estimated from model flat-spectrum radio luminosity functions found in the literature. Dunlop & Peacock (1990, hereafter DP90) derived flat-spectrum radio luminosity functions based on redshift measurements of hundreds of flat spectrum radio sources with $S_{2.7} > 100$ mJy. Specifically, DP90 presented five free-form radio luminosity functions and two parametric radio luminosity functions (i.e. a pure luminosity-evolution model and a model with both luminosity evolution and density evolution). Waddington et al. (2001) tested the DP90 models against the redshift data for a Leiden Berkeley Deep Survey (LBDS) Hercules sample with $S_{1.4} > 1$ mJy. Waddington et al. (2001) find that the measured redshifts for the LBDS Hercules sample are consistent with two of the DP90 models, namely free-form model number 4 (FF-4) and free-form model number 5 (FF-5). Fig. 3 displays the measurements by McKean et al. (in preparation) and the predictions by the DP90 FF-4 and FF-5 models for the differential number–flux-density relation for flat-spectrum radio sources for $S_5 > 1$ mJy. As shown in Fig. 3, for flux densities below 30 mJy the measurements by McKean et al. (in preparation) are roughly consistent with the extrapolation by the DP90 FF-5 model but inconsistent with the DP90 FF-4 model.

Independent pieces of available evidence that can be used to estimate the redshift distribution of the CLASS sources are concordant. Based on spectroscopic observations of a representative subsample of 42 CLASS sources with flux densities from $S_5 = 25$ –50 mJy, Marlow et al. (2000) obtained a mean redshift $\langle z \rangle = 1.27$ with a dispersion of 0.95, at a completeness level of 64%. Since the DP90 FF-4 and FF-5 models are consistent with the LBDS redshift data with $S_5 \gtrsim 1$ mJy (see above), we are allowed to use the DP90 FF-4 and FF-5 models to infer mean redshifts for flat-spectrum sources with $S_5 \gtrsim 1$ mJy. Fig. 4 shows the mean redshift for flat-spectrum sources as a function of flux density predicted by the DP90 FF-4 and FF-5 models. Fig. 4 also shows results from various existing redshift observations of flat-spectrum radio sources, including the Marlow et al.

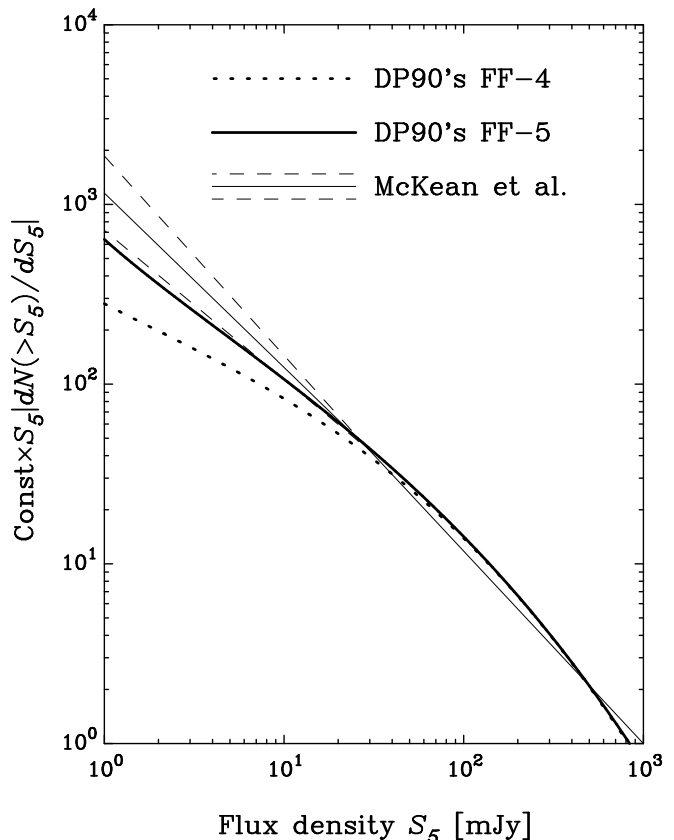


Figure 3. Differential number–flux-density relation $|dN(>S_5)/dS_5|$ for flat-spectrum radio sources. The measurement by McKean et al. (in preparation) is compared with the predictions by DP90’s FF-4 and FF-5 models (see section 3.2).

(2000) result and the results by Falco, Kochanek, & Muñoz (1998), Henstock et al. (1997), and Jackson et al. (2002). From Fig. 4 we see that the prediction by the DP90 FF-5 model agrees well with the independent data while the DP90 FF-4 model is marginally inconsistent with the data, simi-

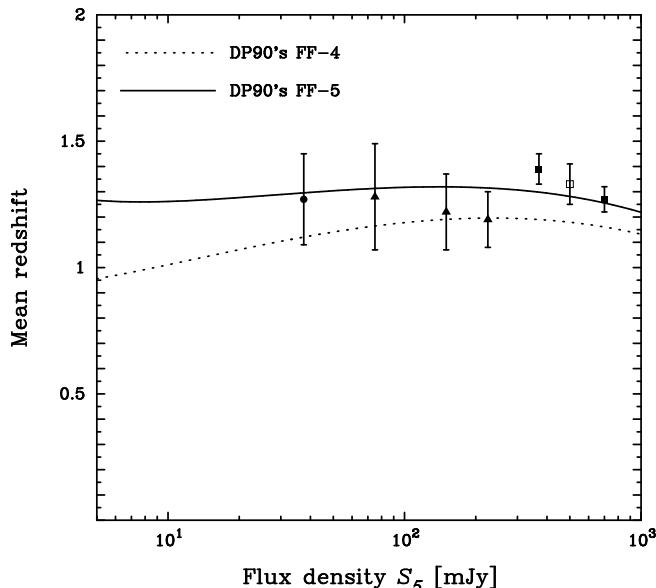


Figure 4. Mean redshifts of flat-spectrum radio sources as a function of flux density. The measured mean and its 1σ error from various observations are shown using a filled dot (CLASS subsample; Marlow et al. 2000), filled triangles (Falco, Kochanek, & Muñoz 1998), filled squares (Parkes quarter-Jansky sample; Jackson et al. 2002), and an open square (the second Caltech-Jodrell Bank sample; Henstock et al. 1997). The predictions by DP90’s FF-4 and FF-5 models (see section 3.2) are respectively shown using dotted and solid lines.

larly to the case for the differential number–flux-density relation (see above). This agreement increases our confidence in the Marlow et al. (2000) measured mean redshift for the CLASS sample. Therefore, we adopt the measurement by Marlow et al. (2000) for a mean redshift for the CLASS sources; i.e., we take a mean $\bar{z} = 1.27 \pm 0.18$ where the estimated error is from the measured dispersion 0.95.

Given that there are only 26 unbiased CLASS sources that have measured spectroscopic redshifts (Marlow et al. 2000), the distribution of the redshifts of the CLASS sources is poorly known. However, since mean redshifts for flat-spectrum sources are nearly the same for various samples regardless of their flux density ranges, as shown in Fig. 4, we may combine the samples assuming that the redshift distributions of the samples are similar. The combined sample comprising the samples shown in Fig. 4 has 747 flat-spectrum source redshifts with $S_5 \gtrsim 30$ mJy. A histogram of the 747 redshifts is shown in Fig. 5. Figure 5 also shows redshift distributions predicted by the DP90 FF-4 and FF-5 models as well as a Gaussian model whose peak redshift and width are determined from the mean and dispersion measured by Marlow et al. (2000). From Fig. 5 we see that the Gaussian model adequately describes the redshift distribution for the combined sample. Therefore, we adopt the Gaussian model to approximate the redshift distribution of the CLASS sources.

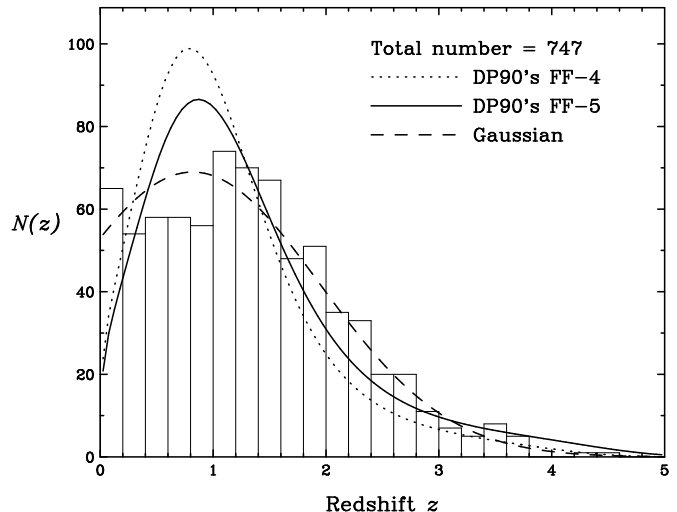


Figure 5. Redshift distribution of flat-spectrum sources. Redshift distributions predicted by the DP90 FF-4 and FF-5 models given for $S_5 = 50$ mJy and a Gaussian model distribution (see section 3.2) are overplotted on a histogram of 747 flat-spectrum source redshifts from various observations (Henstock et al. 1997; Falco, Kochanek, & Muñoz 1998; Marlow et al. 2000; Jackson et al. 2002).

3.3 Galaxy luminosity functions per morphological type and their evolution since $z \sim 1$

Use of reliable galaxy luminosity functions (LFs) is vital in analyses of statistical lensing. For example, use of an underestimated (overestimated) comoving number density of galaxies would mislead us to overestimate (underestimate) a dark energy density. In particular, given that galaxy populations of different morphological types contribute to multiple imaging in distinctively different ways (see section 2.1.3), it is required that type-specific galaxy LFs are reliably determined. For this reason, in this subsection we thoroughly review recent observational results on galaxy LFs and obtain estimates of the early-type and the late-type LFs based on the data from the recent literature. We consider first the estimation of the local type-specific LFs and then review recent observational studies on the evolution of early-type galaxies since $z \sim 1$.

We consider two approaches for estimating the local type-specific LFs. The first approach is to estimate the local total LF and decompose it into an early-type LF and a late-type LF. The second approach is to simply adopt type-specific LFs measured in large-scale galaxy surveys. The advantage of the first approach is that observational information on the total LFs is abundant and now appears to produce a converging result on the total LF, owing to more recent large galaxy redshift surveys particularly including the Sloan Digital Sky Survey (SDSS) and the Two Degree Field Galaxy Redshift Survey (2dFGRS). However, inference of the type-specific LFs from the total LF relies on an independent knowledge of *relative* type-specific LFs. By relative type-specific LFs, we refer to the relative magnitudes of the characteristic number densities of the type-specific LFs. Thus, for the determination of the relative type-specific

LFs, the sample size of the galaxies used is less relevant but the accuracy of the galaxy classification and the photometry are important. Direct use of the measured type-specific LFs from large-scale galaxy surveys in which galaxies were classified (the second approach) suffers from a relatively small number of independent measurements and uncertainties in classifications of large numbers of galaxies in each measurement.

We now consider estimating the total LF taking into account recent data from the literature. Observational results from various past galaxy surveys had systematic differences among the estimates of the local total LF. Not only were the measured values of the three Schechter parameters $M_{*,0}$, α and $n_{*,0}$ significantly different among the various observational results, but also the estimates of the integrated luminosity density given by

$$j_0 = \int_0^\infty dLL \frac{dn(L, z=0)}{dL} = n_{*,0} L_{*,0} \Gamma(\alpha + 2) \quad (45)$$

differed by up to a factor of two.⁸ The past results indicate that, aside from any measurement errors (e.g. photometric errors, missing or misclassification of galaxies), the various determinations of the total LF suffered from large-scale structures in the (local) Universe. The effects of large-scale structures on the determinations of the total LF appear to have caused overall differences between measured LFs based on wide and shallow/sparse surveys (e.g. Loveday et al. 1992; Marzke et al. 1998, hereafter M98) and those based on narrow and deep surveys (e.g. Lilly et al. 1995; Ellis et al. 1996; Geller et al. 1997; Zucca et al. 1997), in the sense that normalisations of the LF for shallow samples are significantly lower than those for deeper samples. Systematic differences in the number counts of galaxies between those towards the northern Galactic cap and the southern Galactic cap also provide evidence of large-scale structures (Yasuda et al. 2001; Norberg et al. 2001). Thus, past determinations of the total LF depended, to a varying extent, on the coordinates defining the sky patches observed in the surveys as well as the angular areas and depths of the surveys.

However, several recent galaxy surveys contain large numbers of galaxies because of the large areas and/or great depths of the surveys. In addition, for a few of the recent galaxy surveys, CCD-based images of galaxies were used to measure the galaxy LFs. More importantly, the results from several reliable observations appear to be concordant. We consider the 2dFGRS (Cross et al. 2001, Norberg et al. 2001), the SDSS (Blanton et al. 2001, Yasuda et al. 2001), the Century (Brown et al. 2001), the ESP (ESO Slice Project; Zucca et al. 1997), and the LCRS (Las Campanas Redshift Survey; Lin et al. 1996) surveys. The 2dFGRS (Cross et al. 2001, Norberg et al. 2001), the SDSS (Blanton et al. 2001, Yasuda et al. 2001), and the LCRS (Lin et al. 1996) observations contain large numbers of galaxies (over 10,000 galaxies each). The SDSS (Blanton et al. 2001; Yasuda et al. 2001), the Century (Brown et al. 2001),

and the LCRS (Lin et al. 1996) observations use CCD-based photometry. Furthermore, the SDSS (Blanton et al. 2001; Yasuda et al. 2001) and the Century (Brown et al. 2001) observations use multiple passbands. All of the above recent surveys except for the LCRS survey (Lin et al. 1996) are based on passbands similar to the Johnson-Morgan B passband in wavelength coverage. The measured values of the Schechter parameters and the luminosity density (equation 45) from these recent surveys are summarized in Table 2. Notice that the characteristic magnitudes for all the above surveys except for the LCRS are quoted in the b_J photometric system using the relevant photometric conversions quoted in the table.

The Norberg et al. (2001) result was obtained by normalising their LF to the combined galaxy number counts from the 2dFGRS southern and northern Galactic caps (over 110,500 galaxies). Likewise, the Yasuda et al. (2001) result was obtained by correcting the LF calculated by Blanton et al. (2001) to match the number counts of galaxies in SDSS ($\sim 900,000$ galaxies). The Norberg et al. (2001) result included modelling and correcting for galaxy evolutionary effects, and the SDSS results were derived using Petrosian magnitudes of galaxies (see Blanton et al. 2001), which overcome dependences of isophotal magnitudes on the surface-brightness distribution of galaxies. The Norberg et al. (2001) and the Yasuda et al. (2001) results are independent of and consistent with each other and probably represent present best estimates of the local total LF. The results of the Century (Brown et al. 2001) and the ESP (Zucca et al. 1997) surveys are also consistent with the Norberg et al. (2001) and the Yasuda et al. (2001) results; however, their statistical errors are larger. The result of the LCRS (Lin et al. 1996), which is based on an R passband, appears to be significantly different from those of the other surveys. We consider the LCRS (Lin et al. 1996) because of the large comoving volume covered by the survey and the fact that it is one of the few CCD-based imaging surveys. While the characteristic magnitude and normalisation of the LF depend on the wavelength coverage of the passband used, recent determinations of LFs at multiple passbands based on CCD photometry did not show any evidence for dependence of the faint-end slope on passbands of optical wavelengths (Blanton et al. 2001; Brown et al. 2001). Thus, the significantly shallower faint-end slope obtained from the LCRS (Lin et al. 1996) compared with those from the other surveys given in Table 2 might appear to be a significant obstacle to a concordant total LF. However, using the SDSS data, Blanton et al. (2001) illustrate dependences of the chosen isophotal limits on the derived LF parameters. In particular, Blanton et al. (2001) argue that the result of Lin et al. (1996) was significantly affected by their chosen relatively bright isophotal limit. We use the Norberg et al. (2001) result and the Yasuda et al. (2001) result to estimate the Schechter parameters of the local total LF. Although the errors of the three Schechter parameters may be correlated, we ignore such correlations and calculate weighted means of the values of the parameters obtained by Norberg et al. (2001) and Yasuda et al. (2001). This result is our estimate of the local total LF given in Table 2.⁹

⁸ Differences in the measurements of each Schechter parameter are in part due to degeneracies among the three Schechter parameters in fitting the data. However, the calculated quantity given by equation (45) would not be significantly affected by such degeneracies.

⁹ We notice that our estimate of the Schechter parameters is also

Table 2. Summary of recent measurements of the local total luminosity function (1. Cross et al. 2001; 2. Norberg et al. 2001; 3. Blanton et al. 2001; 4. Yasuda et al. 2001; 5. Brown et al. 2001; 6. Zucca et al. 1997; 7. Lin et al. 1996)

#	Survey	$M_{*,0} - 5 \log_{10} h$	α	$n_{*,0}$ ($10^{-2} h^3 \text{ Mpc}^{-3}$)	j_0 ($10^8 h L_{\odot} \text{ Mpc}^{-3}$)
1	2dFGRS	-19.75 ± 0.05 (b_J)	-1.09 ± 0.03	2.02 ± 0.02	2.24 ± 0.12
2	2dFGRS	-19.66 ± 0.07 (b_J)	-1.21 ± 0.02	1.68 ± 0.08	1.90 ± 0.18
3	SDSS	-19.71 ± 0.05 (b_J) ^a	-1.26 ± 0.05	2.06 ± 0.23	2.57 ± 0.34
4	SDSS	-19.71 ± 0.05 (b_J) ^a	-1.26 ± 0.05	1.81 ± 0.16	2.26 ± 0.26
5	Century	-19.5 ± 0.09 (b_J) ^b	-1.07 ± 0.09	2.0 ± 0.3	1.74 ± 0.32
6	ESP	$-19.61^{+0.06}_{-0.08}$ (b_J)	$-1.22^{+0.06}_{-0.07}$	2.0 ± 0.4	2.19 ± 0.48
7	LCRS	-20.29 ± 0.02 (R_{KC})	-0.70 ± 0.05	1.9 ± 0.1	1.4 ± 0.1
	Our estimate	-19.69 ± 0.04 (b_J)	-1.22 ± 0.02	1.71 ± 0.07	2.02 ± 0.15

^a The SDSS g^* magnitude was converted to the b_J magnitude using $b_J = g^* + 0.12 + 0.16(B - V)$ and $B - V = 0.94$ (Norberg et al. 2001)

^b The Century V magnitude was converted to the b_J magnitude using $b_J - R = 1.2$ and $V - R = 0.53$ (Brown et al. 2001).

To extract type-specific LFs from our estimated total LF, we define the ratio of the integrated luminosity density of a population of galaxies of type g ($g = e, s$) to the total integrated luminosity density, i.e.,

$$\zeta_0^{(g)} \equiv \frac{j_0^{(g)}}{j_0} = \frac{n_{*,0}^{(g)}}{n_{*,0}} 10^{0.4(M_{*,0} - M_{*,0}^{(g)})} \frac{\Gamma(\alpha^{(g)} + 2)}{\Gamma(\alpha + 2)}, \quad (46)$$

where the last equality follows from equation (45). Notice that the fractional luminosity density given by equation (46) is unaffected either by an error in the absolute photometry or large-scale galaxy-number-density fluctuations. The accuracy in the measurement of the fractional luminosity density in a survey is limited mainly by errors in relative photometry and errors in the galaxy classification. It follows from equation (46) that the type-specific normalisation $n_{*,0}^{(g)}$ is given by

$$n_{*,0}^{(g)} = \zeta_0^{(g)} n_{*,0} 10^{0.4(M_{*,0}^{(g)} - M_{*,0})} \frac{\Gamma(\alpha + 2)}{\Gamma(\alpha^{(g)} + 2)}. \quad (47)$$

Given an estimate of the total LF, independent estimates of parameters $\alpha^{(g)}$ and $M_{*,0}^{(g)}$ along with the the fractional luminosity density $\zeta_0^{(g)}$ will allow us to estimate the type-specific normalization $n_{*,0}^{(g)}$ using equation (47).

We now consider direct measurements of the early-type Schechter parameters from recent galaxy surveys and derive corrected early-type Schechter normalisations using equation (47) from the directly measured early-type Schechter parameters and our estimate of the total LF given in Table 2. Direct measurements of the early-type LF from galaxy surveys are relatively few and have relatively larger uncertainties mainly because of the challenging observational task of accurately classifying large numbers of galaxies. The observational techniques of classifying galaxy types used in various galaxy surveys are based on morphological appearances, surface brightness profiles, prototype spectra, spectral energy distributions, and/or colours of galaxies. Identifying early-type galaxies based on morphological appearances or surface brightness profiles is probably the most reliable method, since the morphological appearances and the

light profiles of spirals, which constitute the most numerous population, are well distinguished from those of early-types. We consider the results from the Second Southern Sky Redshift Survey (SSRS2; M98) and the 2dFGRS (Folkes et al. 1999; Madgwick et al. 2001).¹⁰ The SSRS2 (M98) is a wide-angle, shallow ($z \leq 0.05$) survey of 5404 galaxies in the northern and southern Galactic caps that are brighter than $m_B = 15.5$. The relatively bright magnitude limit used for the SSRS2 allowed M98 to classify the galaxies in their sample through the visual inspection of morphological appearances with more than 99% completeness. M98’s determination of the early-type LF probably represents the best estimate of the local early-type LF. However, as they discuss, the M98 sample would not provide a fair number density of galaxies because the relatively small volume covered by their sample suffers from large-scale density fluctuations. In this respect, the M98 result would only be valuable as a relative early-type LF. M98’s measured values of the local early-type LF parameters can be found in Table 3.

Apart from the M98 study, recent observational studies on galaxy LFs per type did not classify galaxies through morphological appearances but used classification techniques that are based on photometric and spectroscopic information on galaxies (e.g. Folkes et al. 1999; Blanton et al. 2001; Fried et al. 2001; Madgwick et al. 2001; Bernardi et al. 2003). We consider the results by Folkes et al. (1999) and Madgwick et al. (2001) which are based on the 2dFGRS data. Folkes et al. (1999) and Madgwick et al. (2001) have employed the so-called ‘‘principal component analysis (PCA)’’ of galaxy spectra, which essentially maximally quantifies differences between the spectra of galaxies. Kochanek, Pahre, & Falco (2000) have recently argued that the physical properties of apertures (particularly their

¹⁰ An estimate of the Schechter parameters per galactic type is not yet reported from the SDSS, although some classifications of galaxies have been considered (Blanton et al. 2001; Bernardi et al. 2003). In particular, we note that the sample of early-type galaxies used by Bernardi et al. (2003) in their study of early-type galaxies were selected too stringently (for example, luminosities of galaxies in the sample spread over only 4 magnitudes in the brightest range) and thus not suitable to derive a ‘fair’ LF of early-type galaxies.

Table 3. Summary of estimates of the local early-type luminosity function (1. M98; 2. Folkes et al. 1999; 3. Madgwick et al. 2001). The normalisations in the original survey results are corrected using equation (47) and the total luminosity function (Table 2).

#	Survey	$M_{*,0}^{(e)} - 5 \log_{10} h$	$\alpha^{(e)}$	$\zeta_0^{(e)}$	$n_{*,0}^{(e)}$ ($10^{-2} h^3 \text{ Mpc}^{-3}$)	$j_0^{(e)}$ ($10^8 h L_\odot \text{ Mpc}^{-3}$)
1	SSRS2	$-19.63_{-0.11}^{+0.10} (b_J)^a$	-1.00 ± 0.09	0.30 ± 0.08	0.44 ± 0.08	0.41 ± 0.09
	normalisation corrected				0.64 ± 0.19	0.60 ± 0.19
2	2dFGRS	$-19.61 \pm 0.09 (b_J)$	-0.74 ± 0.11	0.34 ± 0.06	0.90 ± 0.09	0.75 ± 0.10
	normalisation corrected				0.82 ± 0.17	0.68 ± 0.15
3	2dFGRS	$-19.59 \pm 0.05 (b_J)$	-0.54 ± 0.02	0.40 ± 0.04	0.99 ± 0.05	0.79 ± 0.05
	normalisation corrected				1.01 ± 0.13	0.81 ± 0.11

^a The $B(0)$ magnitude of SSRS2 was converted to b_J magnitude using $b_J = B - 0.28(B - V)$ (Blair & Gilmore 1982; Norberg et al. 2001) and assuming $B(0) = B$ (Alonso et al. 1993) and mean $(B - V) = 0.94$ (Norberg et al. 2001).

sizes) used for spectroscopic observations in various galaxy redshift surveys are significant sources of systematic errors in galaxy classifications. More generally, those techniques will give correct results only up to the accuracy of the assumed relation between the morphological types and (the parameters used to describe) the spectra of galaxies. Indeed, applying spectrum-based classification techniques to a sample of 4000 2dFGRS galaxies whose morphological types are visually known, Madgwick (2003) finds that the rates of successfully classifying early-type and late-type galaxies by spectrum-based classification techniques range from $\sim 60\%$ - 80% . Nonetheless, the results by Folkes et al. (1999) and Madgwick et al. (2001) are some of the few relatively more reliable results that are available. The values of the Schechter parameters for the local early-type galaxy population obtained by Folkes et al. (1999) and Madgwick et al. (2001) can be found in Table 3. In Table 3, the corrected early-type normalisations using equation (47) can also be found next to each survey result. While the corrected normalization is higher for the SSRS2 result, it is essentially not changed either for the Folkes et al. (1999) result or the Madgwick et al. (2001) result. This implies that the total luminosity densities measured by Folkes et al. (1999) and Madgwick et al. (2001) are consistent with our estimate while that measured by M98 is lower than our estimate. In section 4, we will use for our analyses the corrected SSRS2 (M98) early-type LF and the early-type LF directly measured by Madgwick et al. (2001).

Since the total luminosity density is dominated by late-type galaxies, we assume that the faint-end slope and the characteristic absolute magnitude for late-type galaxies are the same as those for all galaxies, namely we take $\alpha^{(s)} = -1.22 \pm 0.02$ and $M_{*,0}^{(s)} = -19.69 \pm 0.04 (b_J)$. Under this prescription, the normalisation for the late-type population is the same as the ratio of the luminosity density of the late-type population to the total luminosity density. Hence the inferred normalisations for the late-type population are $n_{*,0}^{(s)} = 1.20 \pm 0.11 10^{-2} h^3 \text{ Mpc}^{-3}$ for the M98 type-specific LFs, $n_{*,0}^{(s)} = 1.13 \pm 0.09 h^3 \text{ Mpc}^{-3}$ for the Folkes et al. (1999) type-specific LFs, and $n_{*,0}^{(s)} = 1.03 \pm 0.08 10^{-2} h^3 \text{ Mpc}^{-3}$ for the Madgwick et al. (2001) type-specific LFs.

Finally, it is required that galaxy evolution (of relevance to lensing) be incorporated in the analyses of statistical lensing because the lensing probability is sensitive to the redshift of the potential lensing galaxy (Turner, Ostriker & Gott 1984). Since the lensing rate is dominated by early-type

galaxies, the most relevant issue of galaxy evolution in statistical lensing is whether there is any significant change in the comoving number density of early-type galaxies at most likely lens redshifts (i.e. $z \sim 0.6$) compared with the present epoch as would be the case in certain rapid-evolution models (e.g. Baugh, Cole, & Frenk 1996). There exist in the literature two qualitatively different kinds of observational results on the formation and evolution of early-type galaxies, each of which supports an extreme view of the formation and evolution of early-type galaxies; namely, an early formation by the monolithic collapse of protogalactic gases followed by passive evolution (Eggen, Lynden-Bell & Sandage 1962) or a continuous formation through merging of subunits in a hierarchical structure-formation model (Larson 1974; White & Rees 1978). Galaxy count results that are consistent with the early formation and passive evolution of early-type galaxies appear to be favoured (Im et al. 1996, 1999, 2002; Schade et al. 1999; Totani & Yoshii 1998; Lilly et al. 1995) while some results would support a rapid evolution of early-type galaxies since an intermediate to high redshift (Fried et al. 2001; Kauffmann, Charlot & White 1996). Results from the analysis by the fundamental plane of a sample of gravitational-lens early-type galaxies (Kochanek et al. 2000) would not be consistent with a rapid evolution of early-type galaxies but would be consistent with the early formation and passive evolution hypothesis. A further review of the current status on the formation and evolution of early-type galaxies can be found in Peebles (2002), who argues for the early formation and passive evolution of early-type galaxies based on numerous lines of observational studies such as the colour-magnitude relation and the fundamental plane. Following Peebles (2002) and the authors mentioned above who argue for passive evolution of early-type galaxies, it will be assumed in this study that the local early-type LF has not evolved in the sense that the characteristic comoving number density and the faint-end slope of the early-type LF are unchanged in the lookback times.

4 RESULTS

The results on cosmological parameters and global properties of galaxies that we derive in this section are under the following two key assumptions:

- A galaxy as a gravitational lens is assumed to be well-approximated by a singular isothermal ellipsoid mass model.

Furthermore, dynamical normalisations of lenses are only considered for the oblate and the prolate cases.

- The early-type comoving characteristic number density and faint-end slope are assumed to be unchanged from $z \sim 1$ to the present epoch.

We emphasize that the above assumptions are valid at least as a first-order approximation according to the majority of current evidence (section 2.1; section 3.3). The parameters of our statistical lensing model are summarized in section 2.1.3. Our goals are to constrain cosmological parameters and the early-type characteristic velocity dispersion (and the late-type characteristic velocity dispersion) and the mean projected mass ellipticity of (early-type) galaxies from the observed properties of statistical lensing (given in section 3.1). To meet our goals, we need to fix the rest of the parameters because there exist degeneracies in the total parameter space with the observed properties of statistical lensing. Recent advanced observations have determined the fixed parameters with relatively small uncertainties, as given in section 3.2, section 3.3, and below. Nonetheless, uncertainties in some parameters remain possible sources of systematic errors in the derived results and are discussed in sections 4.3 and 5.3.

The fixed parameters are as follows: (1) both the early-type and the late-type LF faint-end slopes and characteristic number densities as given in section 3.3 (note, however, that two alternative choices of the type-specific LFs are used; see below); (2) the Faber-Jackson exponent $\gamma_{\text{FJ}} = 4.0$ (Bernardi et al. 2001) and the Tully-Fisher exponent $\gamma_{\text{TF}} = 2.9$ (Tully & Pierce 2000) (these parameters affect relatively weakly constraints on galaxy velocity dispersions and consequently cosmological parameters within their present uncertainties); (3) the parameters describing the redshift distribution and the differential number-flux-density relation for the CLASS sources as given in section 3.2 (systematic uncertainties arising from the uncertainties in these parameters will be estimated separately). As simplifications of our analyses, we use a common mean projected mass ellipticity $\bar{\epsilon}$ and a common relative frequency of the oblatenesses \mathcal{P}_{obl} both for the early-type and the late-type populations. The mean ellipticity and the intrinsic shape distribution of late-type galaxies have little effect on our derived results (other than the dependence of the derived late-type characteristic velocity dispersion on these parameters), so we simplify our analyses by using the above prescriptions. The parameters that are allowed to be free are as follows: (1) the cosmological parameters; matter density Ω_{m} , density of a classical cosmological constant Ω_{Λ} or dark energy density Ω_{x} with its constant equation of state w ; (2) the early-type and the late-type characteristic velocity dispersions $\sigma_{*}^{(e)}$ and $\sigma_{*}^{(s)}$; (3) the mean projected mass ellipticity of (early-type) galaxies $\bar{\epsilon}$ and the relative frequency of the oblatenesses \mathcal{P}_{obl} in the intrinsic shape distribution of (early-type) galaxies. We emphasize that it is not only justified but also very sensible to treat the characteristic velocity dispersions (in particular $\sigma_{*}^{(e)}$) as free parameters and determine them from the observed image separations in the final statistical sample. This is because the observed radio-image separations are very accurate and as can be seen from equation (35), image separation has a strong sensitivity on velocity dispersion but little on cosmological parameters in particular within the ranges to be considered below.

While we allow the early-type and the late-type characteristic velocity dispersions to be free, a characteristic central stellar velocity dispersion $\sigma_{\text{c}*,0}^{(e)}$ (at the present epoch) for the early-type population can be obtained through a measured Faber-Jackson relation from the early-type characteristic absolute magnitude, and a characteristic maximum rotation speed $v_{\text{max}*,0}^{(s)}$ (at the present epoch) for the late-type population can also be obtained through a measured Tully-Fisher relation from the late-type characteristic absolute magnitude. The early-type characteristic central stellar velocity dispersion and the late-type characteristic maximum rotation speed (obtained in the above ways) can then be used to estimate the early-type and the late-type characteristic velocity dispersions, although the conversions are model-dependent. Below we use these methods to obtain independent estimates of the early-type and the late-type characteristic velocity dispersions. Such estimates can be compared with the derived values from the statistical lensing model fitting. Furthermore, we will use the estimated late-type characteristic velocity dispersion as a prior constraint for a model fitting in section 4.1. This choice of model fitting is motivated because there is only one confirmed late-type lensing galaxy in the final CLASS statistical sample that can be used to constrain the late-type characteristic velocity dispersion.

The local early-type characteristic absolute magnitude of $M_{*,0}^{(e)}(b_J) - 5 \log_{10} h = -19.61$ along with $B = b_J + 0.26$ (section 3.3) corresponds to a characteristic central stellar velocity dispersion of $\sigma_{\text{c}*,0}^{(e)} = 192 \pm 34 \text{ km s}^{-1}$ through $-M_B = A + 9(\log_{10} \sigma_{\text{c}} - 2.3)$ with a mean $A = 19.5 \pm 0.7$ for both ellipticals and S0 galaxies (expressed for $h = 1$; de Vaucouleurs & Olson 1982). By fitting the observed light distributions and the observed velocity dispersion profiles of 37 elliptical galaxies using singular isothermal mass distributions, Kochanek (1994) finds that the central stellar velocity dispersion of an elliptical galaxy is a good measure of the velocity dispersion of a singular isothermal mass model. Following Kochanek (1994), we thus estimate that $\sigma_{*,0}^{(e)} \approx \sigma_{\text{c}*,0}^{(e)} = 192 \pm 34 \text{ km s}^{-1}$. Alternatively, using the ‘Faber-Jackson’ relation for the dark matter velocity dispersion (i.e., the $\sigma_{\text{DM}}-L$ relation) shown in Fig. 4 of Kochanek (1994), we find that the above early-type characteristic absolute magnitude corresponds to an early-type characteristic velocity dispersion of $\sigma_{*,0}^{(e)} = 185_{-7}^{+9} \text{ km s}^{-1}$.

We adopt the following Tully-Fisher relation to obtain a characteristic velocity dispersion $\sigma_{*,0}^{(s)}$ for the late-type population (Tully & Pierce 2000):

$$-M_B^c = 7.27[\log_{10}(2v_{\text{max}}^{(s)}) - 2.5] + 20.11, \quad (48)$$

where $v_{\text{max}}^{(s)}$ is the maximum rotation speed (i.e. for the edge-on view) and M_B^c is the extinction-corrected absolute B magnitude (i.e., the magnitude for the face-on view), which is given by

$$M_B^c = M_B^{\text{ob}} - \{1.57 + 2.75[\log_{10}(2v_{\text{max}}^{(s)}) - 2.5]\} \log(a/b), \quad (49)$$

where M_B^{ob} is the uncorrected absolute magnitude and a/b is the apparent major-to-minor axis ratio. From $M_{*,0}^{(s)}(b_J) - 5 \log_{10} h = -19.69 \pm 0.04$ along with $B = b_J + 0.26$ (section 3.3) and $h = 0.72 \pm 0.08$ (Freedman et al. 2001), we obtain the characteristic maximum rotation speed of $v_{\text{max}*,0}^{(s)} = 189_{-15}^{+17} \text{ km s}^{-1}$ using equations (48) and (49) and

taking a mean $a/b = 2$. If we assume an SIS mass distribution for the halo of a late-type galaxy, this characteristic maximum rotation speed corresponds to the characteristic velocity dispersion of $\sigma_{*,0}^{(s)} = v_{\max,*,0}^{(s)}/\sqrt{2} = 134_{-10.6}^{+12}$ km s⁻¹.

As discussed at length in section 3.3, while recent observational determinations of the total galaxy luminosity function give a converging result, the decomposition of the total luminosity function by morphological type is less certain. For this uncertainty, we do our analyses for the two choices of the type-specific galaxy LFs, i.e. the normalisation-corrected SSRS2 type-specific LFs and the 2dFGRS type-specific LFs (see Table 3 and section 3.3). The SSRS2 type-specific LFs¹¹ will be our standard choice because their galaxies were classified through visual identifications (see section 3.3), and the 2dFGRS type-specific LFs will be our alternative choice. Notice that the SSRS2 early-type LF has a significantly lower characteristic number density and a significantly steeper faint-end slope compared with the 2dFGRS early-type LF [i.e. $n_{*,0}^{(e)}/(10^{-2} h^3 \text{Mpc}^{-3}) = 0.64 \pm 0.19$ vs. 0.99 ± 0.05 and $\alpha = -1.00 \pm 0.09$ vs. -0.54 ± 0.02].

4.1 Constraints on cosmological parameters

We first consider cosmological models with a classical cosmological constant in which the cosmological parameters to be constrained are the matter density Ω_m and the cosmological constant density Ω_Λ . In other words, we only consider a fixed constant equation of state for dark energy, $w = -1$. Notice, however, that even if we allow w along with Ω_m and Ω_Λ to be varied simultaneously, the constraints on the Ω_m - Ω_Λ plane would change little because the best-fitting value of w is -1 (with the prior constraint $w \geq -1$ imposed) at least for cosmological models that are near the flat line $\Omega_m + \Omega_\Lambda = 1$. We then consider flat cosmological models with a dark energy whose equation of state is assumed to be constant and satisfies the energy condition $w \geq -1$. In this case, the cosmological parameters to be constrained are the matter density $\Omega_m (= 1 - \Omega_x)$ and the constant dark-energy equation of state. Notice here that because of degeneracy on the Ω_m - Ω_Λ plane along a line that is nearly orthogonal to the flat line for a given value of w , it is useful to impose the constraint $\Omega_m + \Omega_\Lambda = 1$.

Fig. 6 shows confidence limits in the parameter plane spanned by Ω_m and Ω_Λ . At each grid point on the plane the value of the χ^2 (equation 44) is determined by minimizing the function over the nuisance parameters (i.e., all the other free parameters). The four contours respectively correspond to 68%, 90%, 95%, and 99% confidence limits for one parameter, namely $\Delta\chi^2 = 1.0, 2.71, 4.0,$ and 6.63 from the global minimum value of the χ^2 , χ_{\min}^2 . Notice that the adopted method for estimating confidence limits on model parameters is the so-called (profile) likelihood ratio method which is one of the widely practiced methods [see, e.g., Lupton (1993) and references therein]. This method gives more conservative (i.e. larger) confidence intervals than the frequently practiced method in which nuisance parameters are held fixed at their global maximum-likelihood values. The confidence intervals obtained by the likelihood ratio method also closely

resemble realistic confidence intervals obtained by projecting the n-dimensional confidence region onto the parameter subspace of interest. However, while computation of the likelihood distribution in the n-dimensional (in the present case 5-dimensional) parameter space is costly even for a moderately grained grid, distribution of likelihood in one or two-dimensional parameter subspace can be computed easily using an efficient optimization routine such as the downhill simplex method (see Press et al. 1992). Here and throughout in this paper all the confidence limits on model parameters are based on the likelihood ratio method. However, we also compute a likelihood distribution in a pseudo full-dimensional grid. By the likelihood distribution in a pseudo full-dimensional grid we shall mean the likelihood distribution in the subspace spanned only by the most crucial parameters where each likelihood value is obtained by fixing the rest of the parameters at their maximum-likelihood values. For the case under consideration, the most crucial three parameters are Ω_m , Ω_Λ , and $\sigma_*^{(e)}$. The pseudo full-dimensional likelihood distribution is available at the Jodrell Bank Observatory web page for gravitational lenses and the CLASS.¹² The web page also includes (profile) likelihood distributions in parameter planes.

Fig. 6 (a) and (b) are the results based on the SSRS2 type-specific LFs while Fig. 6 (c) and (d) are those based on the 2dFGRS type-specific LFs. For the results of Fig. 6 (b) and (d), the late-type characteristic velocity dispersion is constrained by the value obtained from the Tully-Fisher relation (see above).

Fig. 7 shows the w - Ω_m plane in flat cosmology. As in Fig. 6, four different results are presented in Fig. 7 depending on the type-specific LFs and the assumption on the late-type characteristic velocity dispersion. In Table 4, we summarize the 68% and the 95% confidence limits on the cosmological parameters. For the models considered in Fig. 6 and Fig. 7, the fitted values of the early-type characteristic velocity dispersion are somewhat different for the different early-type luminosity functions. Confidence limits on galactic parameters including the early-type characteristic velocity dispersion are presented next in section 4.2.

4.2 Constraints on global properties of galaxy populations

In deriving constraints on galactic parameters, cosmological parameters are varied to minimize the χ^2 (equation 44) at each grid point. Thus, the derived constraints on galactic parameters depend on the allowed ranges of cosmological parameters. In this section, we only consider flat cosmology (i.e. $\Omega_m + \Omega_x = 1$) with $0 < \Omega_m \leq 1$ and fix the dark-energy equation of state w at $w = -1$ (which is the best-fit value when it is allowed to vary with the constraint $w \geq -1$).

Fig. 8 shows confidence limits in the parameter plane spanned by the early-type characteristic velocity dispersion $\sigma_*^{(e)}$ and the late-type characteristic velocity dispersion $\sigma_*^{(s)}$. The six different results in Fig. 8 are for the three different cases of the intrinsic shape distribution of galaxies, i.e. all oblate, one half oblate and the other half prolate, and all prolate, each for the SSRS2 and the 2dFGRS type-specific

¹¹ Hereafter, ‘SSRS2 type-specific LFs’ always refer to the normalisation-corrected SSRS2 type-specific LFs.

¹² <http://www.jb.man.ac.uk/research/gravlens/numerical/numerical.html>

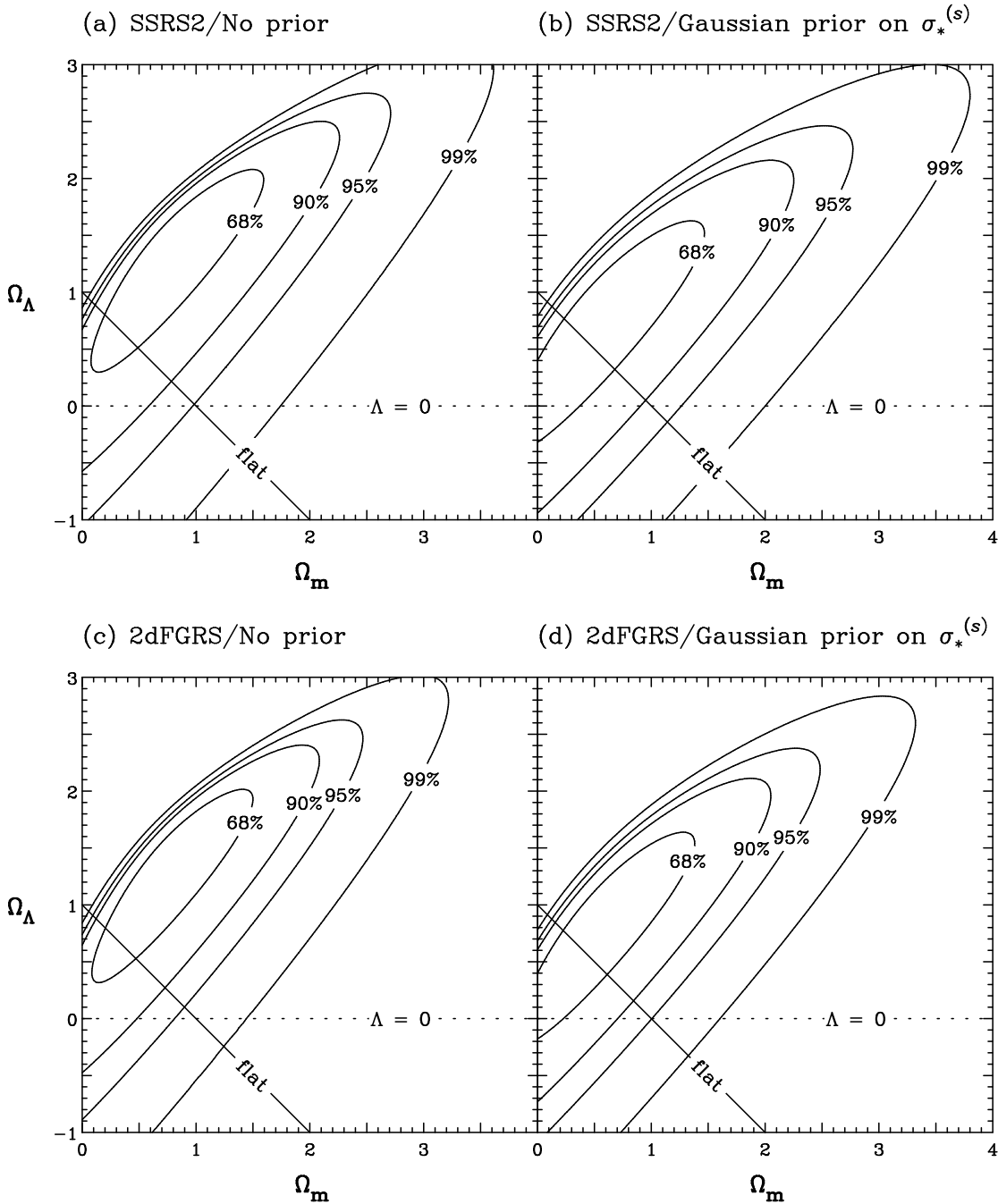


Figure 6. Likelihood regions in the Ω_m - Ω_Λ plane. The four contours, respectively, correspond to the 68%, 90%, 95%, and 99% confidence limits using the $\Delta\chi^2$ (or, likelihood ratio) statistic for one parameter. The four illustrated models are as follows. Models (a) and (b) are based on the SSRS2 type-specific LFs while models (c) and (d) are based on the 2dFGRS type-specific LFs. For models (a) and (c), no prior constraints are imposed on the nuisance parameters while for models (b) and (d), $\sigma_{*,0}^{(s)} = 134^{+12}_{-10.6}$ km s $^{-1}$ (see section 4) in conjunction with the dynamical normalisation for the equal frequencies of oblates and prolates is used as a prior constraint assuming $\sigma_*^{(s)} = \sigma_{*,0}^{(s)}$.

LFs. Fig. 9 shows the parameter plane spanned by the mean projected mass ellipticity of galaxies $\bar{\epsilon}$ and the early-type characteristic velocity dispersion $\sigma_*^{(e)}$ for the same six cases considered in Fig. 8. In Table 5, we summarize the 68% and the 95% confidence limits on the galactic parameters.

4.3 Systematic effects of varying the parameters for the source population

The results presented in sections 4.1 and 4.2 were derived assuming the present best estimates of the redshift distribution and the differential number–flux-density relation for

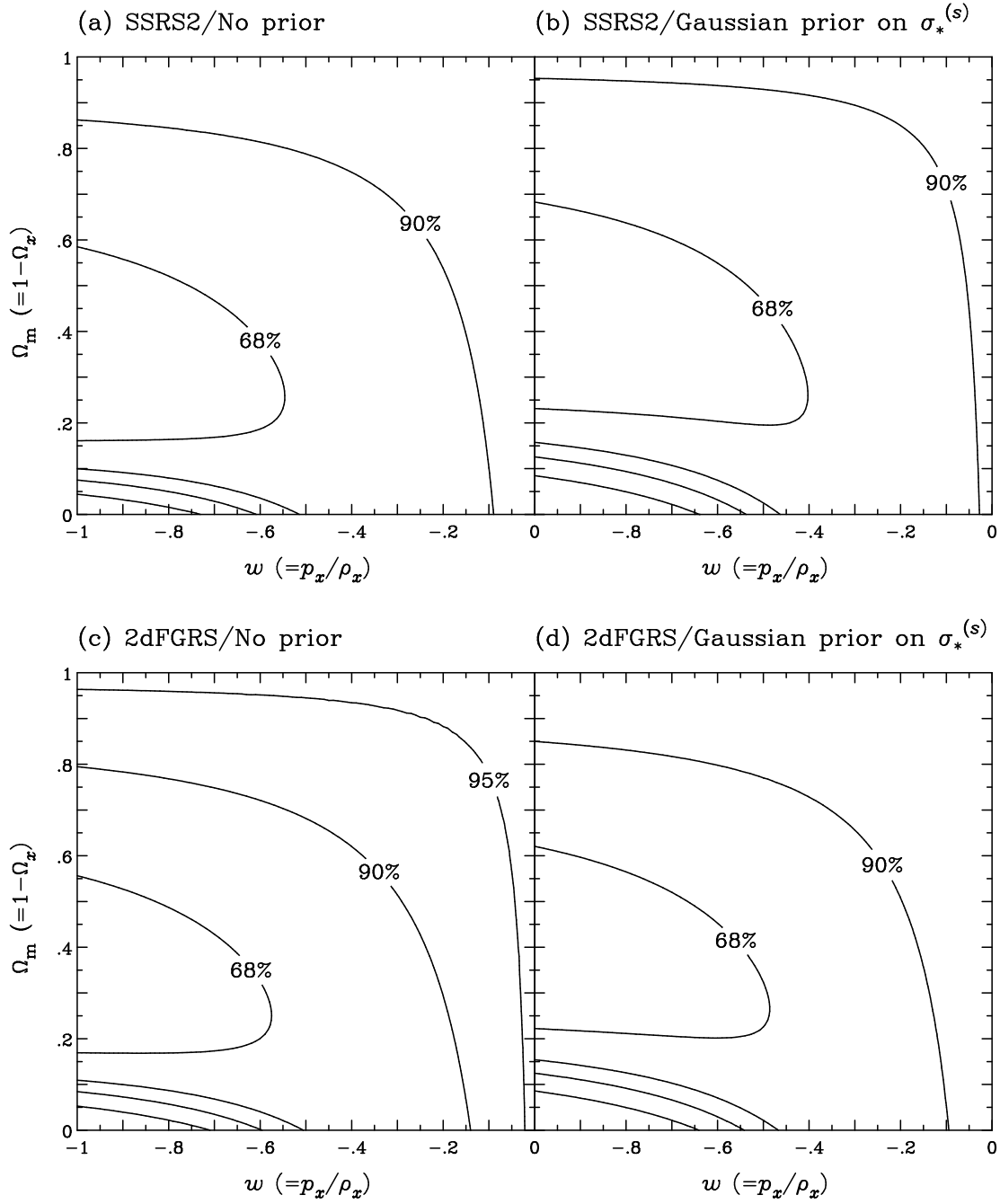


Figure 7. Likelihood regions in the w - Ω_m plane with the prior that the universe is flat for the same models illustrated in Fig. 6.

Table 4. Constraints on cosmological parameters for the four models illustrated in Fig. 6 and Fig. 7.

Model	$\Omega_\Lambda - 1.2\Omega_m$			$\Omega_m (=1 - \Omega_\Lambda)$			w	MLE ¹	68% limit	95% limit
	MLE ¹	68% limit	95% limit	MLE ¹	68% limit	95% limit				
(a)	0.40	(-0.16, 0.73)	(-1.17, 0.92)	0.31	(0.17, 0.58)	(0.08, 1.06)	-1	< -0.55	—	—
(b)	0.12	(-0.50, 0.50)	(-1.52, 0.74)	0.40	(0.24, 0.68)	(0.13, 1.14)	-1	< -0.41	—	—
(c)	0.40	(-0.10, 0.71)	(-0.98, 0.90)	0.31	(0.17, 0.55)	(0.09, 0.96)	-1	< -0.58	< -0.03	—
(d)	0.17	(-0.36, 0.52)	(-1.21, 0.75)	0.38	(0.23, 0.62)	(0.13, 1.00)	-1	< -0.49	—	—

¹ Maximum likelihood estimate which is the value minimizing the χ^2 given by equation (44).

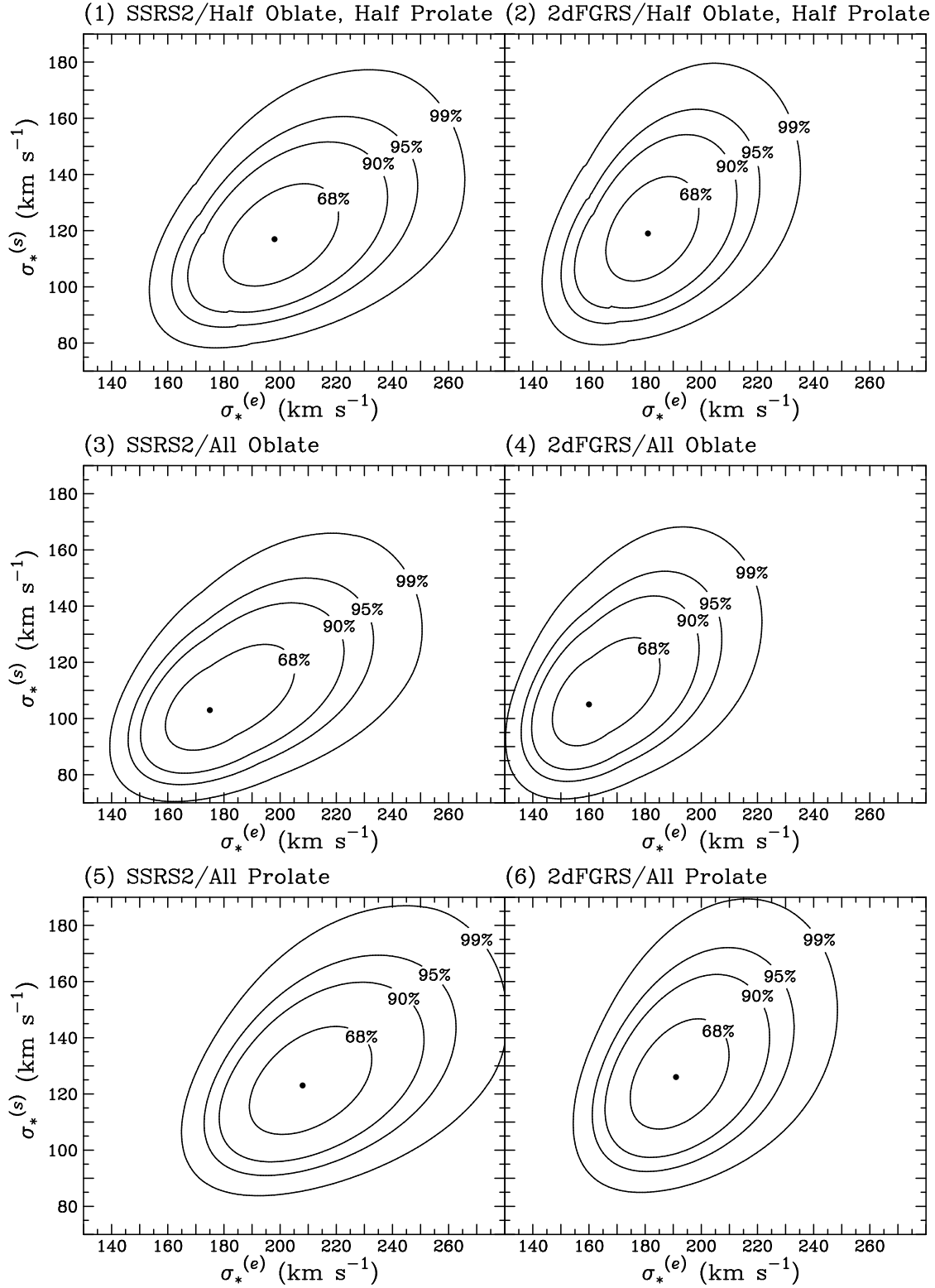


Figure 8. Likelihood regions in the $\sigma_*^{(e)}$ - $\sigma_*^{(s)}$ plane with the prior that the universe is flat, $w = -1$, and $0 < \Omega_m \leq 1$. Models (1), (3), and (5) are based on the SSRS2 type-specific LFs while models (2), (4), and (6) are based on the 2dFGRS type-specific LFs. For models (1) and (2), one half of the galaxies of each type are assumed to be oblate while the other half are assumed to be prolate. For models (3) and (4) all galaxies are assumed to be oblate while for models (5) and (6) all galaxies are assumed to be prolate.

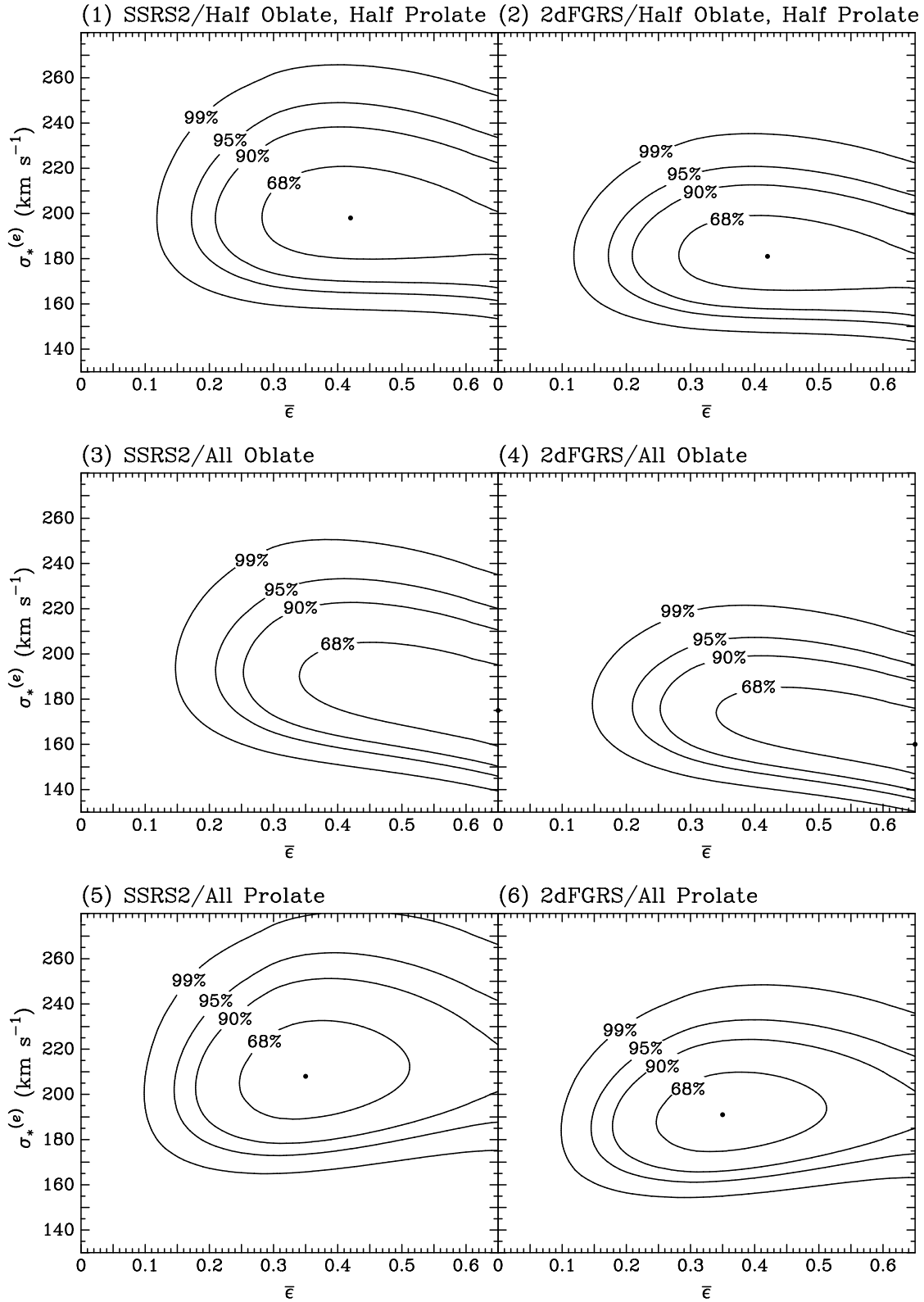


Figure 9. Likelihood regions in the $\bar{\epsilon}$ - $\sigma_*^{(e)}$ plane for the same models illustrated in Fig. 8.

Table 5. Constraints on galactic parameters in flat cosmology for the six models illustrated in Fig. 8 and Fig. 9.

Model	$\sigma_*^{(e)}$ (km s ⁻¹)			$\sigma_*^{(s)}$ (km s ⁻¹)			\bar{e}		
	MLE ¹	68% limit	95% limit	MLE ¹	68% limit	95% limit	MLE ¹	68% limit	95% limit
(1)	198	(180,220)	(162,248)	117	(101,136)	(86,160)	0.42	(0.28,—)	(0.17,—)
(2)	181	(166,199)	(151,220)	119	(103,139)	(87,163)	0.42	(0.28,—)	(0.17,—)
(3)	175	(160,205)	(146,233)	103	(89,126)	(77,149)	—	(0.34,—)	(0.21,—)
(4)	160	(147,185)	(136,207)	105	(91,128)	(78,152)	—	(0.34,—)	(0.21,—)
(5)	208	(190,232)	(173,262)	123	(106,144)	(91,169)	0.35	(0.25,0.51)	(0.14,—)
(6)	191	(175,209)	(162,233)	126	(108,146)	(93,172)	0.35	(0.25,0.51)	(0.14,—)

¹ Maximum likelihood estimate which is the value minimizing the χ^2 given by equation (44).

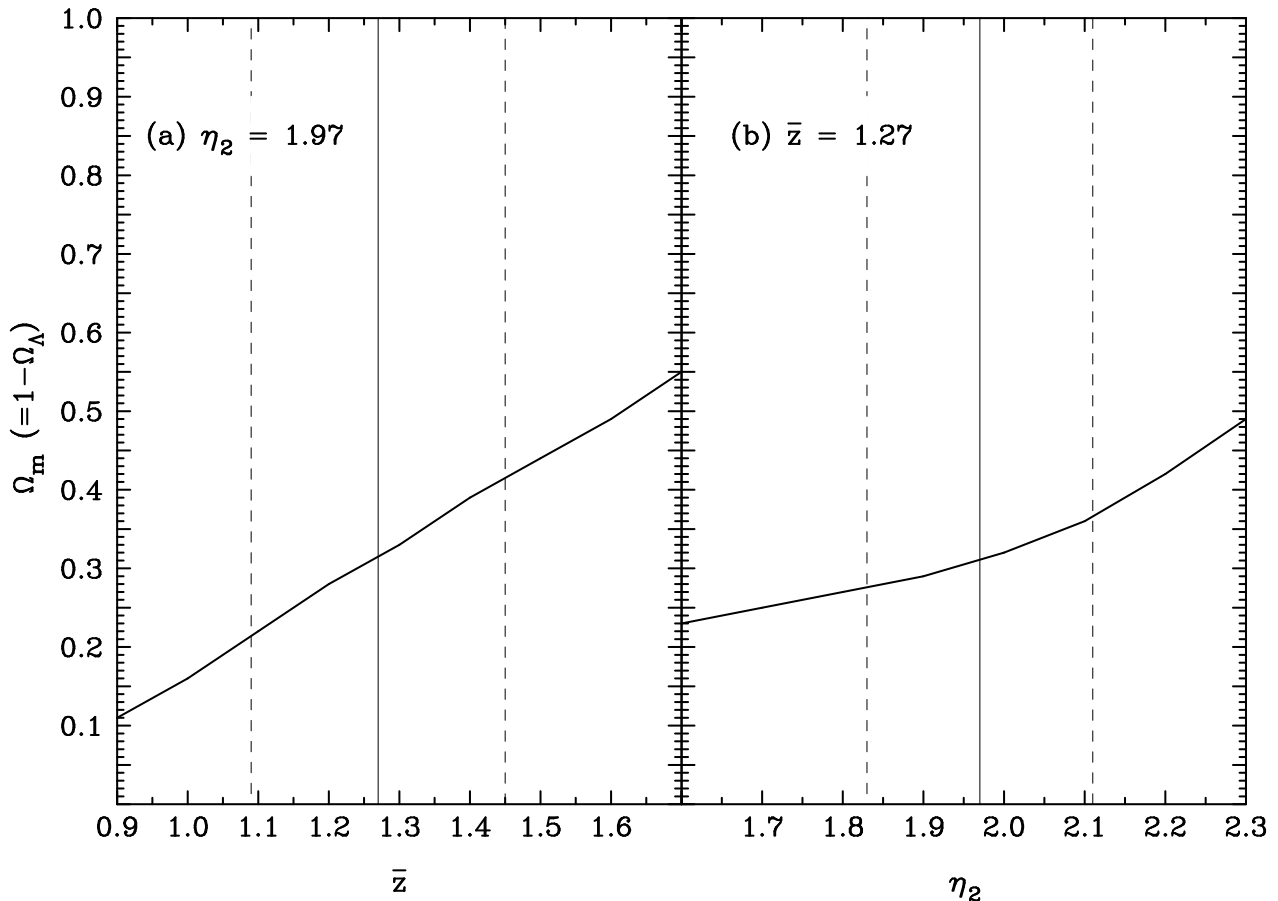


Figure 10. Systematic effects of varying (a) the mean source redshift, \bar{z} and (b) the $|dN/dS|$ slope for $S < 30$ mJy, η_2 , on the maximum likelihood value of Ω_m in flat cosmology with $w = -1$. The thin vertical solid lines, respectively, correspond to the present best estimates of \bar{z} and η_2 while the thin vertical dashed lines correspond to their present uncertainties.

the CLASS sources as given in section 3.2. In other words, the present uncertainties in the redshift distribution and the differential number–flux–density relation for the CLASS sources were not incorporated in the results in sections 4.1 and 4.2. Here we quantify the effects of varying the parameters used to describe the CLASS source population. The source parameters that can have significant impacts on the derived results on the cosmological parameters are the mean redshift, \bar{z} and the differential number–flux–density relation slope for flux densities lower than 30 mJy, η_2 (section 3.2). Figure 10 (a) and (b) show respectively the effects of varying

the parameters \bar{z} and η_2 on the maximum likelihood value of Ω_m in flat cosmology with $w = -1$.

5 DISCUSSION

5.1 Understanding the sensitivities of the model parameters to the observed properties of statistical lensing

The likelihood function [equation 41; or the χ^2 function (equation 44)] for statistical lensing is a complicated func-

tion of the parameters of the statistical lensing model (section 2.1.3). Moreover, the data are characterized by many properties (section 3) which control the likelihood function. For these reasons, it is not straightforward to see how the cosmological and galactic parameters are constrained by the data. Here we discuss the sensitivities of the model parameters to the properties of the data including numerical tests.

To help us see how the model parameters are constrained by the data, we rewrite the χ^2 function (equation 44) as

$$\chi^2 = \chi_U^2 + \chi_L^2, \quad (50)$$

where χ_U^2 and χ_L^2 are respectively the contributions from the unlensed sources and the lensed sources, which are given by

$$\chi_U^2 = \sum_{k=1}^{N_U} \ln \frac{1}{[1 - \sum_m p_m^{(\text{all})}(k)]^2} \quad (51)$$

and

$$\chi_L^2 = \sum_{l=1}^{N_L} \ln \frac{1}{[\delta p_{m_l}^{(\text{one})}(l)]^2}, \quad (52)$$

where the integrated lensing probability $p_m^{(\text{all})}(k)$ and the differential lensing probability $\delta p_{m_l}^{(\text{one})}(l)$ are given by equations (42) and (43). From equations (51) and (52), we see that increasing (decreasing) lensing probabilities increases (decreases) χ_U^2 but decreases (increases) χ_L^2 .¹³ The procedure of fitting the model parameters to the data is to minimize the sum of the oppositely behaving χ_U^2 and χ_L^2 by varying the lensing probabilities.

The lensing probabilities depend on many factors including galactic and cosmological factors and the magnification bias factor which depends on the source properties (section 2.1.2). In other words, the lensing probabilities are determined by the combination of all those factors. Accordingly, the lensing probabilities can be varied in a number of different ways of varying the factors. For example, the lensing probabilities can be decreased by reducing the cosmological factors ($\approx \hat{D}(0, z)^2 |d\ell/dz|$), by decreasing σ_* , or even by reducing the cosmological factors and increasing σ_* (in the last case, one of course has to reduce the cosmological factors sufficiently enough to compensate for increasing σ_*). However, different combinations of the factors are distinguished by the differences in their capabilities of fitting the various properties of the data. For example, combining a very large σ_* and a very low value of the cosmological factors can give a ‘correct’ lensing rate, but such a combination is discarded (i.e. it gives a relatively larger χ^2 value) because it does not fit the observed image separation distribution.

Roughly speaking, for a given dynamical normalisation (section 2.1.1), the observed image separations constrain the characteristic velocity dispersions $\sigma_*^{(e)}$ and $\sigma_*^{(s)}$ and the ratio of the numbers of doubles and of quadruples constrains the surface density ellipticity. For these constrained galactic factors and a magnification bias factor determined from the estimated source properties, the cosmological factors are constrained mostly by the ratio of the numbers of the lensed

sources and of the unlensed sources and (much) less significantly by the redshifts of the lenses and of the sources. In practice, the galactic and cosmological factors are, of course, simultaneously varied to minimize the total χ^2 .

In Table 6, we present the calculated values of the χ_U^2 (equation 51) and χ_L^2 (equation 52) along with the fitted key parameters and the predicted lensing rate for the four different models shown in Fig. 7 and Table 4 and two additional models to be compared. For models (a), (b), and (b’), the SSRS2 type-specific LFs are used while for models (c), (d), and (d’), the 2dFGRS type-specific LFs are used. Notice that for models (b) and (d) the late-type characteristic velocity dispersion is constrained using a Gaussian prior, whose contribution to the total χ^2 is, however, not shown in Table 6. For the two additional models (b’) and (d’), the characteristic velocity dispersions are fixed at $\sigma_*^{(e)} = 225 \text{ km s}^{-1}$ and $\sigma_*^{(s)} = 145 \text{ km s}^{-1}$, which are the preferred values in several previous analyses of statistical lensing (e.g. Kochanek 1996a; Falco, Kochanek, & Muñoz 1998; Quast & Helbig 1999; Helbig et al. 1999). As can be seen in Table 6, galaxy populations following the 2dFGRS type-specific LFs with the fitted characteristic velocity dispersions [Model (c)] have the lowest value for the χ^2 . Compared with Model (c), Model (a) in which galaxy populations follow the SSRS2 type-specific LFs have a larger value for the χ^2 by $\Delta\chi^2 = 1.53$. The larger χ^2 value for Model (a) compared with Model (c) is mostly due to the increase in the value of χ_L^2 . The implication for this is that Model (a) does not fit the observed image separation distribution as well as Model (c) does. Likewise, other models presented in Table 6 have larger χ^2 values mainly because of their larger values of the χ_L^2 compared with Model (c). In particular, Models (b’) and (d’), in which the characteristic velocity dispersions are held fixed, have significantly larger χ_L^2 values compared with Model (c) because the predicted mean image separations are discrepant with the observed mean image separation for those models. To show the above, we present in Fig. 11 the predicted image separation distributions for Models (a), (b’), (c), and (d’). In Fig. 11 are also displayed the model predicted mean image separations and the observed mean image separation for the multiply-imaged systems whose image separations are used in the fit (see section 3.1). Finally, notice that all the models in Table 6 predict correct lensing rates despite the differences in their capabilities of fitting the observed image separation distribution. This is, of course, the consequence of adjusting the value of Ω_m to fit the observed lensing rate for the fitted (or given) galactic parameters in each model.

From the above examination of the example models, we can summarize how the galactic and cosmological parameters are constrained by the data as follows. For the given type-specific LFs, the observed image separations constrain the characteristic velocity dispersions through the χ_L^2 term and then the observed lensing rate constrains cosmological parameters through the sum of the χ_L^2 and the χ_U^2 terms. Since the lensing rate can be fitted by adjusting cosmological parameters for any given galactic parameters, the lensing rate alone cannot constrain cosmological parameters unless one has *a priori* accurate knowledge of the galactic parameters.

¹³ Quast & Helbig (1999) used example figures to demonstrate this point [see their Figs. (A1) and (A2)].

Table 6. Relative χ^2 values and predicted lensing rates for various models of statistical lensing. The χ^2 is given by $\chi^2 = \chi_{\text{U}}^2 + \chi_{\text{L}}^2$, where χ_{U}^2 (equation 51) and χ_{L}^2 (equation 52) are respectively the contributions from the unlensed sources and the lensed sources. Model (a), (b), (c) and (d) are the four models illustrated in Fig. 7 and Table 4, here for the case of flat cosmology with a classical cosmological constant. Notice that for the above models, the early-type and the late-type characteristic velocity dispersions were fitted. On the other hand, for Model (b') and (d') the velocity dispersions were fixed at $\sigma_*^{(e)} = 225 \text{ km s}^{-1}$ and $\sigma_*^{(s)} = 145 \text{ km s}^{-1}$ (see section 5.1). As for Model (a) and (b), the SSRS2 type-specific LFs were used for Model (b') while as for Model (c) and (d), the 2dFGRS type-specific LFs were used for Model (d').

Model	Ω_{m} ($= 1 - \Omega_{\Lambda}$)	$\sigma_*^{(e)}$ (km s^{-1})	$\sigma_*^{(s)}$ (km s^{-1})	χ_{U}^2	χ_{L}^2	$\chi^2 = \chi_{\text{U}}^2 + \chi_{\text{L}}^2$	$\Delta\chi^2$	\bar{p}^a
(a)	0.31	197.8	116.7	25.17	186.96	212.12	1.53	1/711
(b)	0.40	204.8	130.2	25.46	187.14	212.60	2.01	1/703
(b')	0.65	225.0	145.0	25.89	188.41	214.30	3.71	1/691
(c)	0.31	180.8	119.0	25.08	185.52	210.59	$\equiv 0$	1/713
(d)	0.38	185.5	130.8	25.12	185.83	210.95	0.36	1/712
(d')	0.89	225.0	145.0	25.71	189.70	215.41	4.82	1/696

^a The observed lensing rate is 1/689.

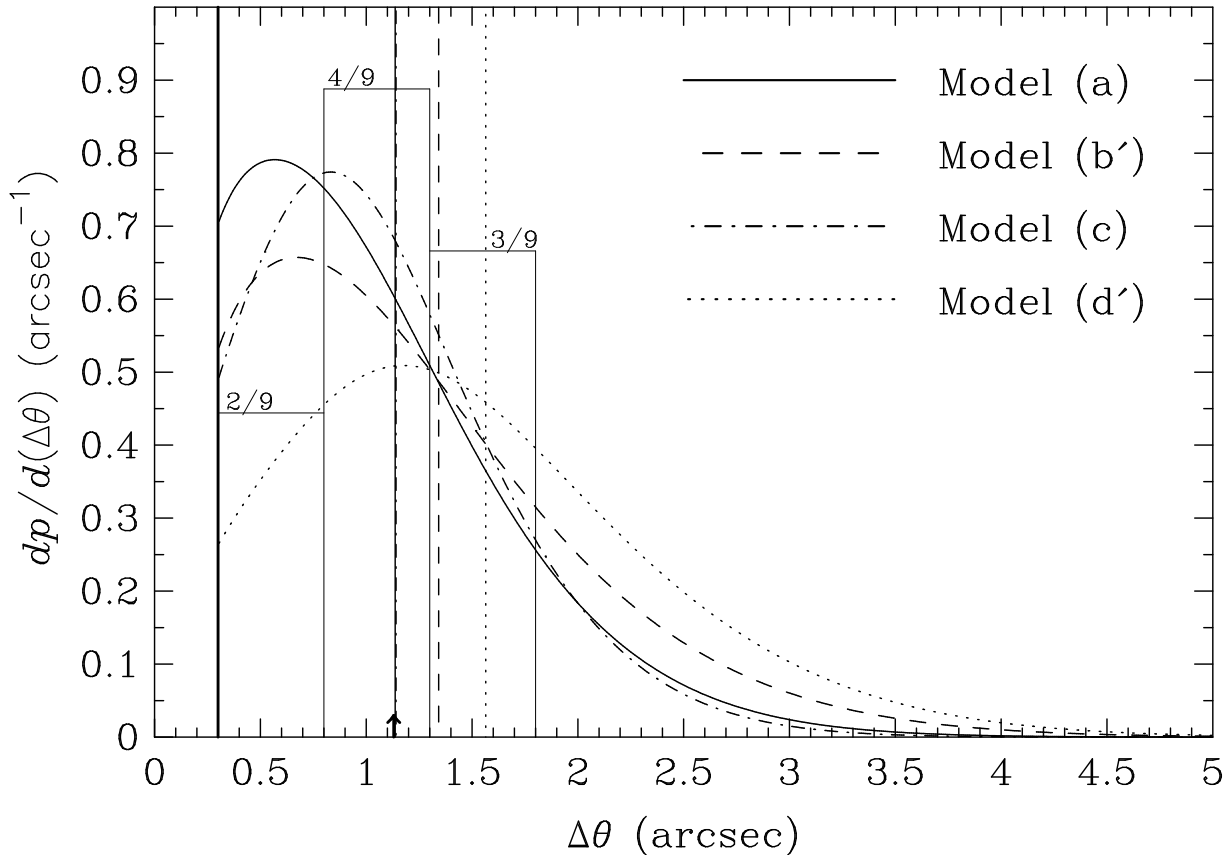


Figure 11. Image separation probability distributions for $\Delta\theta \geq 0.3$ arcsec of multiply-imaged CLASS sources at redshift $z_s = 2$ with lens redshifts $0.3 \leq z_l \leq 1$ (assuming that the unmeasured lens redshifts are also in this range). Theoretical distributions predicted by four models which can be found in Table 6 are overlapped on the observed distribution (i.e. the histogram) of the 9 multiply-imaged sources in the final CLASS statistical sample whose image splittings are known (or likely) to be caused by single galaxies. The small arrow marks the observed mean image separation, namely $(\Delta\theta)_{\text{CLASS}} = 1.13$ arcsec, while the four vertical lines denote the predicted mean image separations of the four models. Notice that the mean image separations predicted by Model (a) and (c), in which the early-type and the late-type characteristic velocity dispersions were fitted, agree well with the observed mean image separation (see section 5.1). The mean image separations predicted by Model (b') and (d'), in which the early-type and the late-type characteristic velocity dispersions were fixed at $\sigma_*^{(e)} = 225 \text{ km s}^{-1}$ and $\sigma_*^{(s)} = 145 \text{ km s}^{-1}$ (see section 5.1), are discrepant with the observed mean image separation. The distribution predicted by Model (c), in which the 2dFGRS type-specific LFs were used, agrees best with the histogram (this explains why the model has the lowest χ^2 value), whose bins, however, consist only of small numbers of data points.

5.2 Comparison with previous results in statistical lensing

Previous analyses of statistical lensing were based on an optically-selected sample, partial samples from radio-selected CLASS sources and other radio-selected sources, and galaxy luminosity functions derived prior to the 2dFGRS and the SDSS observations. The optically-selected sample used for previous analyses is summarized in Kochanek (1996a) and consists of a combined sample of 862 highly luminous QSOs, out of which 5 QSOs are multiply-imaged due to galactic mass-scale lenses. Radio-selected multiply-imaged sources used for previous analyses include 4 multiply-imaged flat-spectrum radio sources (e.g. Helbig et al. 1999) out of a total of 6 JVAS multiply-imaged sources (Browne et al. 2003) and several other multiply-imaged sources including CLASS sources.

Based on the optically-selected sample by Kochanek (1996a) and radio-selected samples, some previous analyses of statistical lensing (Kochanek 1996a; Falco, Kochanek, & Muñoz 1998; Quast & Helbig 1999) obtained limits on Ω_Λ in flat cosmology (or, on $\Omega_\Lambda - \Omega_m$) that would rule out a high Ω_Λ . Most notably, Kochanek (1996a) obtained $\Omega_\Lambda \lesssim 0.66$ a 95% confidence with a maximum likelihood value of $\Omega_\Lambda \sim 0$. This result is significantly different from the results on cosmological parameters that are derived in section 4.1. To understand the results by Kochanek (1996a) and the others mentioned above, it is important to notice that (1) they used for the early-type characteristic velocity dispersion $\sigma_*^{(e)} = 225 \pm 22.5 \text{ km s}^{-1}$ from Kochanek (1994) as a prior information and (2) this prior value of $\sigma_*^{(e)}$ was also consistent with the observed image separations of the multiply-imaged sources used by them for their adopted early-type luminosity function (Kochanek 1996a). The latter point is the consequence of combining two things. First, the mean image separation for the 5 optically-selected lens systems is $\langle \Delta\theta \rangle_{\text{optical}} = 1.60 \text{ arcsec}$ which is significantly larger than the mean separation of $\langle \Delta\theta \rangle_{\text{CLASS}} = 1.13 \text{ arcsec}$ for the 9 multiply-imaged sources (or, $\langle \Delta\theta \rangle_{\text{CLASS}}^{(e)} = 1.23 \text{ arcsec}$ excluding the confirmed spiral lens system 0218+357) in the final CLASS statistical sample (section 3.1) whose image separations are (likely to be) due to single galactic potentials.¹⁴ Second, the fitted value of $\sigma_*^{(e)}$ is a function of the early-type faint-end slope $\alpha^{(e)}$ (for a fixed Faber-Jackson exponent γ_{FJ}) as seen in section 4.2, and the early-type LF used by the above authors has a relatively steep faint-end slope of $\alpha^{(e)} = -1.00 \pm 0.15$ similar to that for the SSRS2 early-type LF (section 3.3) and thus requires a relatively larger value of $\sigma_*^{(e)}$ (compared with a shallower faint-end slope as in the 2dFGRS early-type LF). In passing, we mention that the local early-type characteristic number density $n_{*,0}^{(e)}$ estimated by Kochanek (1996a) agrees well with that for the SSRS2 early-type LF.

Like the above authors, Helbig et al. (1999) adopted $\sigma_*^{(e)} = 225 \pm 22.5 \text{ km s}^{-1}$ in deriving limits on cosmological parameters based on their JVAS sample. Helbig et al. (1999)

obtained $-0.85 < \Omega_\Lambda < 0.84$ at 95% confidence with a maximum likelihood value of $\Omega_\Lambda > 0$ for a flat cosmology. This result is somewhat different from that by Kochanek (1996a) in the sense that it marginally favors a positive Ω_Λ . However, it is also different from the results of this paper (section 4.1) which favor a Ω_Λ -dominated universe. Given the difference between the value of $\sigma_*^{(e)}$ adopted by Helbig et al. (1999) and the values fitted to CLASS lenses (section 4.2), it is perhaps not surprising to find that the Helbig et al. (1999) result and our results are different. Yet, it would be of interest to assess and understand the difference between the Helbig et al. (1999) result and our results more concretely and clearly, especially since the JVAS sample used by Helbig et al. (1999) is a CLASS subsample just as the final CLASS statistical sample is. What if $\sigma_*^{(e)}$ was fitted to the lenses in the Helbig et al. (1999) sample rather than being fixed at $\sigma_*^{(e)} = 225 \text{ km s}^{-1}$? What factors other than the value of $\sigma_*^{(e)}$ (in particular, the more realistic statistical lensing model, the adopted profile likelihood ratio method of estimating parameters and their errors, and sample variance) might be attributed to the difference between the results of Helbig et al. (1999) and of this paper? First of all, we recall that there is no significant difference in galactic parameters other than $\sigma_*^{(e)}$ between Helbig et al. (1999) and this paper. To help us see separately the effects of varying statistical lensing model, parameter and error estimation method, and sample, we consider Fig. 12 which shows four variants of Fig. 6 (a) (i.e., results based on the SSRS2 type-specific LFs). Fig. 12 (a) and (b) are the results based on the same data used by Helbig et al. (1999)¹⁵ but using our model. Fig. 12 (a) is the result obtained considering only early-type galaxies and taking $\sigma_*^{(e)} = 225 \text{ km s}^{-1}$ [i.e., adopting the same approach used by Helbig et al. (1999)]. To obtain Fig. 12 (a), we also assumed that oblates and prolates have equal frequencies (i.e. dynamical normalisation $\lambda \sim 1$) and took a mean projected galaxy mass ellipticity $\bar{\epsilon} = 0.42$ which gives the best-fit to the final CLASS statistical sample (see Fig. 9). Fig. 12 (b) is the result obtained by applying our new approach adopted in this paper to the Helbig et al. (1999) data. This means that both early-type and late-type populations were considered and their characteristic velocity dispersions were fitted to the observed image separations of the Helbig et al. (1999) 4 multiply-imaged systems. Fig. 12 (c) and (d) are the results based on two subsamples of the final CLASS statistical sample (section 3.1) and using the same model and approach adopted in this paper. Fig. 12 (c) is based only on the JVAS subsample within the final CLASS statistical sample which comprises 1749 sources including three multiply-imaged sources 0218+357, 1422+231, and 2114+022. Fig. 12 (d) is based on a subsample of 2308 sources including four multiply-imaged sources 0445+123, 0712+472, 2045+265, and 2319+051 which were randomly selected from the subsample of 7209 sources in-

¹⁴ The radio-selected multiply-imaged sources collected by Kochanek (1996a) and used to constrain $\sigma_*^{(e)}$ have a mean separation of $\langle \Delta\theta \rangle_{\text{radio(Kochanek)}} \approx 1.6$ which is nearly equal to $\langle \Delta\theta \rangle_{\text{optical}}$.

¹⁵ A noticeable difference in sample selection criteria between the Helbig et al. (1999) sample and the final CLASS statistical sample is that the lower limit of the fainter-to-brighter image flux-density ratio for doubly-imaged sources is 0.05 for the Helbig et al. (1999) sample. This was taken into account in deriving the results shown in Fig. 12 (a) and (b).

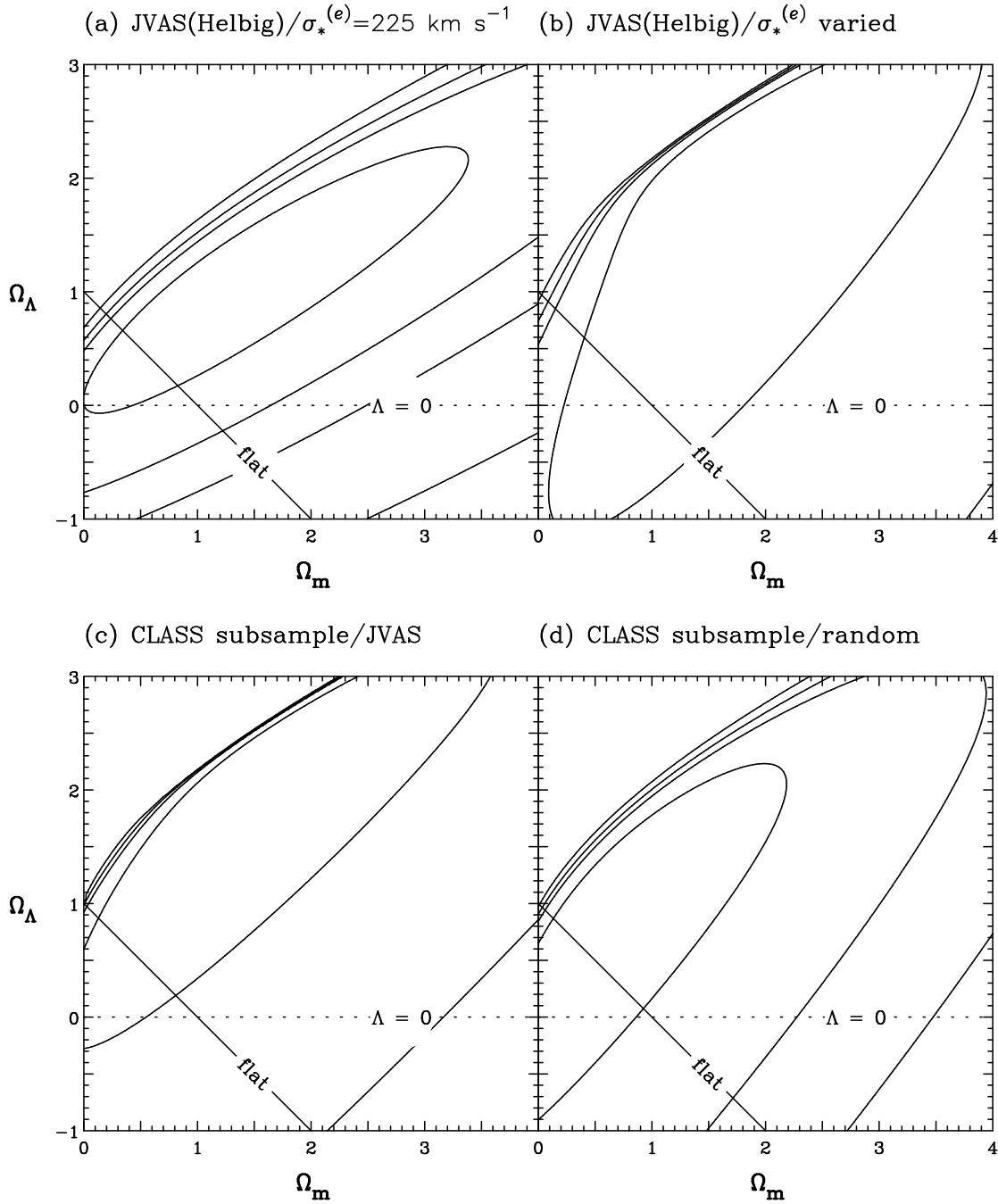


Figure 12. Likelihood regions in the Ω_m - Ω_Λ plane for the SSRS2 type-specific LFs as in Fig. 6(a) based on previous and present subsamples from the entire JVAS and CLASS sources, shown to illustrate the effects of different statistical lensing models, different parameter and error estimate methods, and different samples. The four contours in each panel, respectively, correspond to the 68%, 90%, 95%, and 99% confidence limits for one parameter. (a) & (b) are based on the Helbig et al. (1999) sample; (a) is the result of only fitting the lensing rate fixing early-type characteristic velocity at $\sigma_*^{(e)} = 225 \text{ km s}^{-1}$ whereas (b) is the result of simultaneously fitting both the lensing rate and the image separations. Both (c) and (d) are the results of simultaneously fitting both the lensing rate and the image separations based on subsamples of the final CLASS statistical sample: (c) is the result based on the subsample that comprises only 1749 JVAS sources whereas (d) is based on a random subsample that comprises 2308 non-JVAS sources. The comparison of (a) and Fig. 1 of Helbig et al. (1999) shows the effects of the different statistical lensing models. The comparison of (a) and (b) shows the effects of the different parameter and error estimate methods. The comparison among (b), (c), and (d) shows differences or similarities among samples. Finally, the comparison of (d) [or (c)] and Fig. 6(a) shows the effects of different sample sizes. See section 5.2 for a full discussion of the results.

cluding 10 multiply-images sources within the final CLASS statistical sample that are not JVAS sources.

Let us briefly discuss the implications of the results displayed in Fig. 12. From Fig. 12 (a), we have $\Omega_\Lambda = 0.48_{-0.30}^{+0.16}$ (68%) and $0.48_{-0.98}^{+0.32}$ (95%) for a flat cosmology. This result favors a positive Ω_Λ universe and the difference from the Helbig et al. (1999) result is not significant. Thus, we are led to conclude that the differences in the details of the statistical lensing model (in particular, cross sections and magnification biases) between this paper and Helbig et al. (1999) make little difference in deriving limits on cosmological parameters based on presently available data (i.e. within presently reachable accuracies). From Fig. 12 (b), we have $\Omega_\Lambda = 0.32_{-0.72}^{+0.26}$ (68%) for a flat cosmology. The somewhat lower maximum-likelihood estimate of Ω_Λ from Fig. 12 (b) compared with that from Fig. 12 (a) is the consequence of the early-type characteristic velocity dispersion larger than 225 km s^{-1} fitted to the image separations that are due to early-type galaxies in the Helbig et al. (1999) sample (the mean image separation for 0414+054, 1030+074, and 1422+231 is 1.64 arcsec). Another main difference between Fig. 12 (a) and (b) is that the confidence interval at a given confidence level is much smaller in Fig. 12 (a) although both were based on the same data. This is, of course, due to the fact that $\sigma_*^{(e)}$ was fixed for Fig. 12 (a) while it was varied for Fig. 12 (b) based on the profile likelihood ratio method (see section 4.1). The above comparison of Fig. 12 (a) and (b) shows that different approaches of treating galactic parameters can make significant differences in the derived values of cosmological parameters for the same data. The results displayed in Fig. 12 (c) and (d) are based on the profile likelihood ratio method as in Fig. 12 (b). We have $\Omega_\Lambda = 0.68_{-0.48}^{+0.18}$ and $0.64_{-0.56}^{+0.22}$ at 68% confidence respectively from Fig. 12 (c) and (d). These values of Ω_Λ are very similar to each other but different from the value obtained from Fig. 12 (b). For example, the confidence interval of Ω_Λ implied by the Helbig et al. (1999) data excludes at 68% confidence both of the maximum-likelihood estimates of Ω_Λ shown on Fig. 12 (c) and (d). In other words, even if not at a high statistical significance, the Helbig et al. (1999) data are inconsistent with two subsets of the the final CLASS statistical sample when all three of the data sets are analysed and interpreted in the same manner. This could imply that the Helbig et al. (1999) sample is incomplete within their specified sample definitions or is not as observationally well-defined as the final CLASS statistical sample. Alternatively, the Helbig et al. (1999) sample simply (as a rare occurrence) happens to include the lensed system 0414+054 that has an image separation of 2.09 arcsec and is a main factor behind the low value of Ω_Λ . Comparing Fig. 12 (d) [or Fig. 12 (c)] with Fig. 6 (a), we find that as the sample size becomes four times larger, the 68% confidence interval approximately halves consistent with the expectation for a Poisson error.

In summary, Kochanek (1996a), Helbig et al. (1999) and the other authors above either found or adopted $\sigma_*^{(e)} \approx 225 \text{ km s}^{-1}$, and for this and other adopted galactic parameters the observed lensing rates in the optical sample of QSOs and the JVAS samples of flat-spectrum radio sources were most consistent with relatively low values of Ω_Λ . In particular, some of these authors produced results that even appeared to rule out a high value of Ω_Λ such as $\Omega_\Lambda = 0.7$.

Some previous analyses of statistical lensing were based

on choices of galactic parameters that were different from those used by Kochanek (1996a), Helbig et al. (1999), and the others above. Cooray (1999) used choices of $n_{*,0}^{(e)}$ and $\alpha^{(e)}$ that were similar to those used by Kochanek (1996a) but separated the early-type population into an elliptical (E) population and an S0 population with a number ratio of E: S0 = 1: 1.6 and estimated the characteristic velocity dispersions from his chosen LFs and Faber-Jackson relation as $\sigma_* = 210_{-11}^{+10} \text{ km s}^{-1}$ for the E population and $\sigma_* = 194_{-10}^{+12} \text{ km s}^{-1}$ for the S0 population. The Cooray (1999) estimates of the E and S0 characteristic velocity dispersions correspond to an effective characteristic velocity dispersion for the entire early-type population that is $\gtrsim 1\sigma$ lower than the estimate by Kochanek (1994). Not surprisingly, Cooray (1999) obtained a relatively high upper limit of $\Omega_\Lambda \lesssim 0.79$ at 95% confidence in flat cosmology from the lensing rate in an incomplete subsample of ~ 6500 CLASS sources. Notice, however, that Cooray (1999) did not use the observed image separations in his analysis to test whether the chosen LFs and characteristic velocity dispersions were consistent with them or not.

Choices of galactic parameters that are significantly different from those used by Kochanek (1996a), Cooray (1999), and the others above were considered by Chiba & Yoshii (1999) and Cheng & Krauss (2001). In particular, based on the same lens systems used by Kochanek (1996a), Chiba & Yoshii (1999) found $\Omega_\Lambda \gtrsim 0$ at 98% confidence with a maximum likelihood value of $\Omega_\Lambda \approx 0.7$ because of their radically different choices of galactic parameters. The galactic parameters preferred by Chiba & Yoshii (1999) and Cheng & Krauss (2001) can be characterized by a very shallow or inverted (i.e. positive) faint-end slope for the early-type LF. Furthermore, Cheng & Krauss (2001) argued for a shallow slope of $\gamma \approx 2$ to 3 in the $\sigma_{\text{DM}}-L$ relation for the early-type galaxies, and Chiba & Yoshii (1999) used an early-type characteristic number density [i.e. an early-type LF by Loveday et al. (1992)] that is a factor of ≈ 2 to 3 lower than those in the SSRS2 and the 2dFGRS early-type LFs (Table 3). The shallow/inverted early-type faint-end slopes necessarily require lower values for $\sigma_*^{(e)}$ for the given same image separations compared with a steeper slope (as noted above). The high value for Ω_Λ obtained by Chiba & Yoshii (1999) was the combined effect of the significantly lower values for the early-type characteristic velocity dispersion and number density than those used by Kochanek (1996a). Although the limits on Ω_Λ obtained by Chiba & Yoshii (1999) agree well with the results on cosmological parameters based on the final CLASS statistical sample (section 4.1), we note that (1) the early-type LF used by Chiba & Yoshii (1999) is discrepant with present more reliable early-type LFs (section 3.3) and (2) the statistical lensing samples used by Chiba & Yoshii (1999) (i.e. those collected by Kochanek 1996a) were defined using selection functions that are observationally not as reliable as those used to define the final CLASS statistical sample and thus are more likely to be subject to unknown biases (which may explain the difference in the mean image separations between the final CLASS statistical sample and other samples).

Compared with the observational information that was available to the previous analyses of statistical lensing (in particular those that put limits on cosmological parameters),

the presently available observational information used in this work is more abundant and more reliable. The final CLASS statistical sample is defined so as to satisfy the selection criteria (section 3.1) that are both observationally well-defined and reliable. This means that its biases are well understood and can be accurately taken into account in the analysis of the sample. [For comparison, optically-selected samples suffer from dust extinction which cannot be accurately taken into account for analyses of statistical lensing (see Falco et al. 1999).] The final CLASS statistical sample is the most significant piece of information that has been available only to this work. The total galaxy LFs derived from the 2dF-GRS and the SDSS observations and more recently derived type-specific LFs have now significantly reduced uncertainties in the early-type LF. The fact that the well-defined final CLASS statistical sample and the relatively more reliable early-type LFs were used and all the factors in the statistical lensing model were carefully taken into account based on relatively reliable data and with thorough understanding, makes the results on cosmological parameters reported in Chae et al. (2002) and here (section 4.1) much more reliable than those from previous analyses.

So far in this section, we have focused on cosmological parameters in the comparison with previous analyses of statistical lensing. We now compare our derived results on galactic parameters with those in previous analyses. As emphasized above, the mean image separation in the final CLASS statistical sample is significantly smaller than those in the optical QSO sample and the heterogeneously defined radio-selected samples (Kochanek 1996a). We recall that this was the main reason for the difference in the cosmological constraints between Kochanek (1996a) and this work (section 4.1). The implication for the early-type characteristic velocity dispersion is that it is $\sim 27 \text{ km s}^{-1}$ lower than the estimate by Kochanek (1994) for the steep SSRS2 early-type LF and $\sim 44 \text{ km s}^{-1}$ lower for the shallow 2dF-GRS LF.¹⁶ We point out that this fitted value of the early-type characteristic velocity dispersion is also consistent with our estimate of the early-type characteristic magnitude (section 3.3). Namely, our estimate of the early-type characteristic magnitude $M_{*,0}^{(e)}(B)$ is ~ 0.5 mag fainter than the one adopted by Kochanek (1996a) and it implies $\sigma_{*,0}^{(e)} \sim 190 \text{ km s}^{-1}$ either by a Faber-Jackson relation (de Vaucouleurs & Olson 1982) or a $\sigma_{\text{DM}}-L$ relation (Kochanek 1994) (see section 4).

Our statistical lensing model incorporates the (differential) lensing probabilities of specific image multiplicities for the multiply-imaged sources using the SIE lens model (rather than a circular lens). This allows us to constrain the mean projected mass ellipticity of galaxies from the multiply-imaged sources of well-defined image multiplicities. In section 3.1, we pointed out that 10 systems out of the 13 lens systems in the CLASS statistical sample have well-defined image multiplicities for which single galactic potentials are (likely to be) only responsible. The 10 systems contain 6 doubly-imaged ones and 4 quadruply-imaged ones. The relative frequency of the doubles in the final CLASS statistical sample is similar to (or slightly higher than) those

in the samples used by King & Browne (1996), Kochanek (1996b), and Keeton, Kochanek, & Seljak (1997). However, the relative frequency for the doubles is higher than that in the CLASS subsample used by Rusin & Tegmark (2001), in which there are 5 doubles and 7 quadruples.¹⁷ This difference is for two reasons. First, in the time since Rusin & Tegmark (2001) did their analysis based on CLASS lens systems available at that time, the CLASS group has identified two new lens systems 0445+123 (Argo et al. 2003) and 0631+519, both of which are doubly-imaged systems and are now included in the final CLASS statistical sample. Second, the observational criteria used to define the final CLASS statistical sample (section 3.1) are not only more stringent but more reliable than those used to define the statistical sample used by Rusin & Tegmark (2001). Based on their statistical sample and the SIE lens model, Rusin & Tegmark (2001) concluded that the predicted mean mass ellipticity of the early-type galaxies ($\bar{\epsilon}_{\text{mass}} \approx 0.6$) was much higher than an observed mean light ellipticity. In particular, Rusin & Tegmark (2001) found that the observed ellipticity distribution of the early-type galaxies in the Coma cluster was inconsistent with the relative frequencies of the doubles and the quadruples in their sample at 98% statistical significance.

Based on the final CLASS statistical sample and the SIE lens model, we find that the best-fit mean mass ellipticity for the (early-type) galaxies¹⁸ is $\bar{\epsilon}_{\text{mass}} = 0.42$ (Fig. 9; Table 5) and the 68% lower limit is 0.28 for the dynamical normalisation of the equal frequencies of the oblates and the prolates. For the dynamical normalisation of all oblates, the 68% lower limit is increased to 0.34. For the dynamical normalisation of all prolates, $\bar{\epsilon}_{\text{mass}} = 0.35^{+0.16}_{-0.10}$ at 68%. These results are consistent with the observed mean light ellipticity $\bar{\epsilon}_{\text{light,DEEP/GSS}} \approx 0.38$ (Fig. 18 in Im et al. 2002) for the field early-type galaxies of the Deep Extragalactic Evolutionary Probe (DEEP) Gross Strip Survey (GSS) or $\bar{\epsilon}_{\text{light,Coma}} \approx 0.32$ for the combined E and S0 galaxies in the Coma cluster [Fig. 3(a) in Jørgensen & Franx 1994]. Therefore, the potential ‘ellipticity crisis’ for gravitational lenses that were noticed and investigated in the previous works (Rusin & Tegmark 2001; Kochanek 1996a; King & Browne 1996) based on samples that are not as well-defined as the final CLASS statistical sample, has now significantly weakened.

¹⁷ Rusin & Tegmark (2001), as in this work, did not use compound lenses in which multiple potentials are responsible for the image multiplicities.

¹⁸ Recall that a common mean mass ellipticity for both early-type and late-type populations of galaxies is considered and fitted to the image multiplicities that are generated by both early-type and late-type (appropriately isolated) lensing galaxies. Since most of the lensing galaxies are early-type, the common mean mass ellipticity can be regarded as the mean mass ellipticity of early-type galaxies with little error.

¹⁶ This is based on the dynamical normalisation for the equal numbers of the oblates and the prolates, i.e. $\lambda(f) \approx 1$.

5.3 Possible sources of systematic errors

5.3.1 Mass profiles, intrinsic shapes, and velocity dispersions of galaxies

In this work, we adopted the singular isothermal mass profile and the axisymmetric intrinsic shapes (i.e., oblate and prolate) to model galaxy lenses. We also assumed that the distribution function of a galaxy depends only on the relative energy and the angular momentum component parallel to the symmetry axis of the galaxy. With the adopted mass model and the assumption on the distribution function, we calculated, as functions of apparent axial ratio and line-of-sight velocity dispersion, the multiple-imaging cross sections averaged over all the combinations of intrinsic shapes and inclination angles that are consistent with the apparent axial ratio for the assumed relative frequencies of oblates and prolates. The apparent axial ratio and the characteristic velocity dispersions (corresponding to the characteristic absolute magnitudes) were then constrained by the observed relative frequencies of image multiplicities and the observed image separations in the final CLASS statistical sample. We found that the values of the early-type characteristic velocity dispersion obtained in the way described above agreed well with the values based on the early-type characteristic absolute magnitude and a Faber-Jackson relation or a $\sigma_{\text{DM}}-L$ relation (recall here that a singular isothermal mass profile was also assumed; see section 4). The values of the late-type characteristic velocity dispersion obtained from the statistical lensing analyses were $\approx 1\sigma$ lower than the value based on the late-type characteristic absolute magnitude and a Tully-Fisher relation.

How would the derived results from the statistical lensing analyses be affected if non-isothermal mass profiles, non-axisymmetric intrinsic shapes, and/or general three-integral distribution functions of galaxies were considered? Constraints on cosmological parameters are not likely to be affected by non-isothermal mass profiles, non-axisymmetric intrinsic shapes, or general distribution functions according to the following arguments. For the given apparent axial ratio and line-of-sight velocity dispersion, the cross sections averaged over the allowed ensemble of models obviously depend on the assumed galaxy model. Hence, the derived characteristic velocity dispersions from the observed image separations depend on the mass profile, the allowed range of intrinsic shapes, and the assumption on the distribution function of the galaxy. (Dependences on the intrinsic shapes for the singular isothermal mass profile were illustrated in section 4.) However, while the derived characteristic velocity dispersions are affected as the galaxy model is varied, the multiple-imaging cross sections are not as long as the projected surface density of the inner cylindrical region of the galaxy is similar to the isothermal surface density. In other words, the observed image separations will determine the multiple-imaging cross sections regardless of the details of the galaxy model as long as the image separation for the given multiple-imaging cross section is not significantly dependent on the image magnification ratio, similarly to the case for the singular isothermal profile in which the image separation is fixed by the cross section and independent of the magnification ratio.

5.3.2 Local early-type LF: the characteristic number density and faint-end slope

As discussed in section 3.3, there is no consensus among observationally derived results for the early-type LF. We have used two choices of the early-type LF in this work, namely the steep SSRS2 choice and the shallow 2dFGRS choice. As seen in section 4, while the two different early-type LFs require different values of $\sigma_*^{(e)}$ to fit the same image separations in the CLASS statistical sample, the difference in the values of $n_{*,0}^{(e)}$ for the two early-type LFs is such that the two early-type LFs give similar results on cosmological parameters (Fig. 6 & 7). However, the fact that the two different early-type LFs give similar results on cosmological parameters does not preclude the possibility that the presently derived constraints on cosmological parameters based on the two early-type LFs suffer from systematic errors due to the present uncertainties in the early-type LF. As pointed out in section 3.3, the main difficulty in the observational derivation of the early-type LF lies in classifying large numbers of galaxies by morphological types. Systematically misclassifying galaxies will not only result in an error in the number density of early-type galaxies but also an error in the faint-end slope in the early-type LF. Given that the derived cosmological parameters depend on both the early-type characteristic number density and faint-end slope, it is understood that the presently derived constraints on cosmological parameters are potentially susceptible to unquantified systematic errors due to the present uncertainties in the early-type LF. Nonetheless, since the total galaxy LF has been reliably determined, as long as the partition of the total LF into the type-specific LFs is not drastically different from those considered in this work, the conclusions drawn on cosmological parameters (section 4.1) would not be significantly affected.

5.3.3 Evolution of early-type galaxies

One key assumption made in this work is no evolution of early-type galaxies since $z \sim 1$ in the sense that the early-type characteristic comoving number density and faint-end slope are unchanged from $z \sim 1$ to the present epoch. In section 3.3, we pointed out that the hypothesis of the early ($z \gtrsim 2$) formation and passive evolution of early-type galaxies is supported by many lines of observational studies.

However, the evolution of early-type galaxies remains a relatively larger source of uncertainty for analyses of statistical lensing. First, the observational results that provided the most direct pieces of evidence for little or no evolution of the early-type characteristic comoving number density and faint-end slope were based on relatively small samples of galaxies and were less than abundant. Furthermore, limits on galaxy evolution derived from galaxy counts are dependent on the assumed cosmological model and thus, in a strict sense, should not be used for constraining cosmological parameters via statistical lensing (see, e.g., Keeton 2002). Second, there exist observational results in the literature that have been used to claim a rapid evolution of early-type galaxies in which there is a significant reduction in the comoving number density of early-type galaxies at in-

intermediate redshifts ($0.3 \lesssim z \lesssim 1$) compared with the present epoch.¹⁹

If future observational studies established a rapid evolution in the population of early-type galaxies since $z \sim 1$ so that the comoving number density of early-type galaxies at an intermediate redshift was significantly lower than that at the present epoch, the constraints on cosmological parameters derived in this work would have to be adjusted; the adjustment would increase (decrease) dark energy density (matter density). Reversing the problem, statistical lensing can be used in the future to constrain the formation and evolution of early-type galaxies assuming a certain cosmological model. From the results of this work, the qualitative inference on the formation and evolution of early-type galaxies would be that a flat ‘concordance cosmology’ with $\Omega_m \approx 0.3$ ($\Omega_\Lambda \approx 0.7$) favors an early ($z \gtrsim 1.5$) formation of early-type galaxies followed by passive evolution. A detailed quantitative analysis of statistical lensing focusing on constraining the formation and evolution of early-type galaxies assuming the concordance cosmology will be presented in a forthcoming publication (Mao & Chae 2003).

5.3.4 Redshift distribution of CLASS sources

As shown in Figure 10(a), the derived value of Ω_m (in a flat universe) is sensitive to the mean redshift of CLASS sources. Since the Marlow et al. (2000) measurement has a relatively large uncertainty due to the relatively small number of measured spectroscopic redshifts, it will be important to obtain secure redshifts for more CLASS sources in the future to reduce the uncertainty arising from the current uncertainty in the mean redshift of CLASS sources.

Six multiply-imaged sources in the final CLASS statistical sample (Table 1) lack measured redshifts. While the unknown redshifts would not change the derived results from analyses of statistical lensing as long as they are not too close to their corresponding lens redshifts,²⁰ it would be important to measure them not just as a matter of completeness but to make sure that no surprising results are missed.

6 FUTURE PROSPECTS OF STATISTICAL LENSING

As demonstrated in detail in this work, statistical properties of strong gravitational lensing allow us to probe independently cosmological models and global properties of galaxies. In principle, a sample of cosmologically distant sources that is observationally well-defined and large enough can alone

pin down both cosmological parameters (e.g. Ω_m , Ω_Λ , and ω) and global parameters of galaxies (e.g. $\sigma_*^{(e)}$, early-type velocity function slope, $\sigma_*^{(s)}$, spiral-type velocity function slope, and $\bar{\epsilon}_{\text{mass}}$) including their evolutionary properties. Since determining cosmological parameters and global properties of galaxies is a main and fundamental part of cosmology, it is important to have various independent methods. Statistical lensing provides such a method.

The Cosmic Lens All-Sky Survey is the largest systematic strong gravitational lens survey at the time of this writing. A second Cosmic Lens All-Sky Survey (CLASS2) is being planned and would aim to discover ten times as many multiply-imaged radio-loud sources as the CLASS did. A statistical sample from a CLASS2 project would allow us to measure cosmological and galactic parameters with three times smaller statistical errors compared with the values obtained in this work assuming that the errors are Poissonian [this appears to be the case from the comparison of Fig. 12 (c) or (d) with Fig. 6 (a) (see section 5.2) and we will deal with the issue regarding errors in a future publication through an extensive Monte Carlo simulation of statistical lensing (Chae et al., in preparation)]. For example, this means that statistical lensing could independently come up with a value of Ω_m (or Ω_x) with an error of ~ 0.05 (if a flat universe is assumed) and values of $\sigma_*^{(e)}$ and $\sigma_*^{(s)}$ with errors of $\sim 7 \text{ km s}^{-1}$.

It is almost certain that statistical lensing will not enable us to measure cosmological parameters with the precision that is achievable by cosmic microwave background anisotropy measurements or supernovae observations through space-based instruments for the present and the coming decade [e.g., Wilkinson microwave anisotropy probe (*WMAP*: Spergel et al. 2003); Planck surveyor²¹; supernova/acceleration probe (SNAP)²²]. Nevertheless, independent results on cosmological parameters from statistical lensing are of interest and value because the importance of cosmological parameters warrants demanding tests. However, perhaps the greatest value of statistical lensing for the coming years lies in its unique probe of the velocity functions of galaxies and galaxy evolution. In particular, the velocity dispersions implied by the image separations of strongly-lensed systems are different from those measured spectroscopically from galaxy surveys such as the SDSS, and statistical lensing probes galaxy evolution based on mass-selected samples of galaxies whereas studies from galaxy surveys are based on brightness-selected samples. Thus, statistical lensing provides valuable and unique constraints on theories of the formation and evolution of galaxies.

7 CONCLUSIONS

From the analyses of statistical lensing based on the final CLASS statistical sample, the current estimate of luminosity functions of galaxies per morphological type, and the singular isothermal ellipsoid (SIE) lens model, we have reached the following conclusions:

¹⁹ However, it is interesting to note that those who found a rapid evolution of early-type galaxies classified galaxies through photometric/spectroscopic information (e.g. Fried et al. 2001) while those who found little or no evolution of early-type galaxies classified galaxies through morphological appearances or light profiles (e.g. Im et al. 2002).

²⁰ The uncertain redshift of 2045+265 can be an issue here. The system has the highest lens redshift among the measured lens redshifts and a relatively large image separation. Furthermore, there was an early report that the source redshift could be $z_s = 1.28$ although this interpretation was very uncertain (Fassnacht et al. 1999).

²¹ <http://astro.esa.int/SA-general/Projects/Planck>

²² <http://snap.lbl.gov>

(i) The multiple-imaging cross sections of galaxies implied by the observed image separations are such that the observed ‘local’ distributions of galaxies require a cosmological model dominated by dark energy to be compatible with the observed multiple-imaging rate, under the assumption that field early-type (i.e. E/S0) galaxies existed with the present-epoch abundance and masses at intermediate redshifts $0.3 \lesssim z \lesssim 1$. In particular, the confidence region in the Ω_m - Ω_Λ plane is in good agreement with that from Type Ia supernovae observations (Riess et al. 1998; Perlmutter et al. 1999). This independent result further supports a flat concordance cosmology with $\Omega_m \sim 0.3$ ($\Omega_\Lambda \sim 0.7$). However, if the early-type galaxy population underwent a significant evolution from $z \sim 1$ to the present epoch as in a certain hierarchical galaxy formation picture, the statistical lensing data used in this work would imply an even higher dark energy density.

(ii) Assuming that one half of early-type galaxies are oblates and the other half are prolates, the fitted early-type characteristic line-of-sight velocity dispersion is $\sigma_*^{(e)}(0.3 \lesssim z \lesssim 1) = 198_{-18}^{+22}$ km s⁻¹ (68%) if the early-type LF faint-end slope follows that of the ‘steep’ SSRS2 early-type LF (i.e. $\alpha^{(e)} = -1$), or $\sigma_*^{(e)}(0.3 \lesssim z \lesssim 1) = 181_{-15}^{+18}$ km s⁻¹ (68%) if it follows that of the ‘shallow’ 2dFGRS early-type LF (i.e. $\alpha^{(e)} = -0.54$). These results are consistent with the current estimate of the early-type characteristic absolute magnitude in the *B* band and the σ -*L* relation, but are significantly lower than the previous result based on the optically-selected lens sample and the SSRS2-like steep early-type faint-end slope.

(iii) Assuming that one half of early-type galaxies are oblates and the other half are prolates, the best-fit value for the mean projected mass ellipticity of early-type galaxies is 0.42 and the 68% lower limit is 0.28. The inferred mean projected mass ellipticity agrees well with the measured mean light ellipticity of early-type galaxies in ‘fields’ (i.e., random environments) or in clusters.

ACKNOWLEDGMENTS

This work is the follow-up of, and complementary to, Chae et al. (2002), in which the CLASS team reports constraints on cosmological parameters based on the final CLASS data. As a ‘latest member’ of the CLASS collaboration, the author thanks those who worked hard to produce the final CLASS data. J. McKean et al. are further thanked for their work on CLASS parent source counts. The author particularly thanks Ian Browne and Peter Wilkinson for initial motivational comments that led him to contribute toward the Chae et al. (2002) results and this work. Ian Browne has also provided useful comments on the text. The author thanks the anonymous referee of the paper for a thorough review and numerous constructive comments. In particular, we owe the referee Fig. 12 and relevant discussion. The additional work presented in the revised version was supported by the Astrophysical Research Center for the Structure and Evolution of the Cosmos (ARCSEC) which was established under the Science Research Center (SRC) program of Korea Science and Engineering Foundation (KOSEF).

REFERENCES

- Alonso M. V., da Costa L. N., Pellegrini P. S., Kurtz M. J., 1993, *AJ*, 106, 676
- Argo M. K., et al., 2003, *MNRAS*, 338, 957
- Augusto P., Browne I. W. A., Wilkinson P. N., Jackson N. J., Fassnacht C. D., Muxlow T. W. B., Hjorth J., Jaunsen A. O., Koopmans L. V., Patnaik A. R., Taylor G. B., 2001, *MNRAS*, 326, 1007
- Baugh C. M., Cole S., Frenk C. S., 1996, *MNRAS*, 283, 1361
- Bernardi M., et al., 2003, *AJ*, 125, 1865
- Binney J., Tremaine S., 1987, *Galactic Dynamics*. Princeton Univ. Press, Princeton, NJ
- Blair M., Gilmore G., 1982, *PASP*, 94, 742
- Blanton M., et al., 2001, *AJ*, 121, 2358
- Brown W. R., Geller M. J., Fabricant D. G., Kurtz M. J., 2001, *AJ*, 122, 714
- Browne I. W. A., Patnaik A. R., Walsh D., Wilkinson P. N., 1993, *MNRAS*, 263, L32
- Browne I. W. A., et al., 2003, *MNRAS*, 341, 13
- Carroll S. M., Press W. H., Turner E. L., 1992, *ARA&A*, 30, 499
- Chae K.-H., 2002, *ApJ*, 568, 500
- Chae K.-H., Mao S., Augusto P., 2001, *MNRAS*, 326, 1015
- Chae K.-H., et al., 2002, *PRL*, 89, 151301
- Cheng Y.-C. N., Krauss L. M., 2001, *NewA*, 6, 249
- Chiba M., Yoshii Y., 1999, *ApJ*, 510, 42
- Cooray A. R., 1999, *A&A*, 342, 353
- Cross N., et al., 2001, *MNRAS*, 324, 825
- de Bernardis P., et al., 2002, *ApJ*, 564, 559
- de Vaucouleurs G., Olson D. W., 1982, *ApJ*, 256, 346
- Dunlop J. S., Peacock J. A., 1990, *MNRAS*, 247, 19 (DP90)
- Eggen O. J., Lynden-Bell D., Sandage A. R., 1962, *ApJ*, 136, 748
- Ellis R. S., Colless M., Broadhurst T., Heyl J., Glazebrook K., 1996, *MNRAS*, 280, 235
- Falco E. E., Impey C. D., Kochanek C. S., Lehár J., McLeod B. A., Rix H.-W., Keeton C. R., Muñoz J. A., Peng C. Y., 1999, *ApJ*, 523, 617
- Falco E. E., Kochanek C. S. & Muñoz J. A. 1998, *ApJ*, 494, 47
- Fassnacht C. D., Cohen J. G., 1998, *AJ*, 115, 377
- Fassnacht C. D., et al., 1999, *AJ*, 117, 658
- Folkes S., et al., 1999, *MNRAS*, 308, 459
- Freedman W. L., et al., 2001, *ApJ*, 553, 47
- Fried J. W., von Kuhlmann B., Meisenheimer K., Rix H.-W., Wolf C., Hippelein H. H., Kümmel M., Phleps S., Röser H. J., Thierring I., Maier C., 2001, *A&A*, 367, 788
- Fukugita M., Futamase T., Kasai M., 1990, *MNRAS*, 246, P24
- Fukugita M., Futamase T., Kasai M., Turner E. L., 1992, *ApJ*, 393, 3
- Fukugita M., Turner E. L. 1991, *MNRAS*, 253, 99
- Geller M. J., Kurtz M. J., Wegner G., Thorstensen J. R., Fabricant D. G., Marzke R. O., Huchra J. P., Schild R. E., Falco E. E., 1997, *AJ*, 114, 2205
- Helbig P., Marlow D., Quast R., Wilkinson P. N., Browne I. W. A., Koopmans L. V. E., 1999, *A&AS*, 136, 297
- Henstock D. R., Browne I. W. A., Wilkinson P. N., McMahon R. G., 1997, *MNRAS*, 290, 380
- Im M., Griffiths R. E., Naim A., Ratnatunga K. U., Roche N., Green R. F., Sarajedini V. L., 1999, *ApJ*, 510, 82
- Im M., Griffiths R. E., Ratnatunga K. U., Sarajedini V. L., 1996, *ApJ*, 461, L79
- Im M., Simard L., Faber S. M., Koo D., Gebhardt K., Willmer C. N. A., Phillips A., Illingworth G., Vogt N. P., Sarajedini V. L., 2002, *ApJ*, 571, 136
- Impey C. D., Foltz C. B., Petry C. E., Browne I. W. A., Patnaik A. R., 1996, *ApJ*, 462, L53
- Jackson C. A., Wall J. V., Shaver P. A., Kellermann K. I., Hook I. M., Hawkins M. R. S. 2002, *A&A*, 386, 97
- Jorgensen L., Franx M., 1994, *ApJ*, 433, 553

- Kauffmann G., Charlot S., White S. D. M., 1996, MNRAS, 283, L117
- Keeton C. R., 2002, ApJ, 575, L1
- Keeton C. R., Kochanek C. S., 1998, ApJ, 495, 157
- Keeton C. R., Kochanek C. S., Seljak U., 1997, ApJ, 482, 604
- King L. J., Browne I. W. A., 1996, MNRAS, 282, 67
- King L. J., Browne I. W. A., Marlow D. R., Patnaik A. R., Wilkinson P. N., 1999, MNRAS, 307, 225
- Kochanek C. S., 1993, ApJ, 419, 12
- Kochanek C. S., 1994, ApJ, 436, 56
- Kochanek C. S., 1996a, ApJ, 466, 638
- Kochanek C. S., 1996b, ApJ, 473, 595
- Kochanek C. S., Falco E. E., Impey C. D., Lehár J., McLeod B. A., Rix H.-W., Keeton C. R., Muñoz J. A., Peng C. Y., 2000, ApJ, 543, 131
- Kochanek C. S., Pahre M. A., Falco E. E., 2000, ApJ, submitted (astro-ph/0011458)
- Koopmans L. V. E., Fassnacht, C. D., 1999, ApJ, 527, 513
- Koopmans L. V. E., Treu T., 2003, ApJ, 583, 606
- Kormann R., Schneider P., Bartelmann M., 1994, A&A, 284, 285
- Larson, R. B., 1974, MNRAS, 166, 585
- Lilly S. J., Tresse L., Hammer F., Crampton D., Le Fevre O., 1995, ApJ, 455, 108
- Lin H., Kirshner R. P., Shectman S. A., Landy S. D., Oemler A., Tucker D. L., Schechter P. L., 1996, ApJ, 464, 60
- Liske J., Lemon D. J., Driver S. P., Cross N. J. G., Couch W. J., 2002, MNRAS, submitted (astro-ph/0207555)
- Loveday J., Peterson B. A., Efstathiou G., Maddox S. J., 1992, ApJ, 390, 338
- Lupton, R., 1993, *Statistics in Theory and Practice*. Princeton Univ. Press, Princeton, NJ
- Madgwick D. S., 2003, MNRAS, 338, 197
- Madgwick D. S., et al., 2002, MNRAS, 333, 133
- Mao S., 1991, ApJ, 380, 9
- Mao S., Chae K.-H., 2003, ApJL, submitted
- Mao S., Kochanek C. S., 1994, MNRAS, 268, 569
- Maoz D., Rix H.-W., 1993, ApJ, 416, 425
- Marlow D. R., Rusin D., Jackson N., Wilkinson P. N., Browne I. W. A., Koopmans L., 2000, AJ, 119, 2629
- Marzke R. O., da Costa L. N., Pellegrini P. S., Willmer C. N. A., Geller M. J., 1998, ApJ, 503, 617 (M98)
- Muñoz J. A., Kochanek C. S., Keeton C. R., 2001, ApJ, 558, 657
- Myers S., et al., 1995, ApJ, 447, L5
- Myers S., et al., 2003, MNRAS, 341, 1
- Norberg P., et al., 2002, MNRAS, 328, 64
- Peebles P. J. E., 2002, preprint (astro-ph/0201015)
- Perlmutter S., et al., 1999, ApJ, 517, 565
- Press W. H., Teukolsky S. A., Vetterling W. T., Flannery B. P., 1992, *Numerical Recipes in FORTRAN*. Cambridge Univ. Press
- Qian E. E., de Zeeuw P. T., van der Marel R. P., Hunter C., 1995, MNRAS, 274, 602
- Quast R., Helbig P., 1999, A&A, 344, 721
- Riess A. G., et al., 1998, AJ, 116, 1009
- Rusin D., Kochanek C. S., Norbury M., Falco E. E., Impey C. D., Lehár J., McLeod B. A., Rix H.-W., Keeton C. R., Muñoz J. A., Peng C. Y., 2001a, ApJ, 557, 594
- Rusin D., Marlow D. R., Norbury M., Browne I. W. A., Jackson N., Wilkinson P. N., Fassnacht C. D., Myers S. T., Koopmans L. V. E., Blandford R. D., Pearson T. J., Readhead A. C. S., de Bruyn A. G., 2001b, AJ, 122, 591
- Rusin D., Tegmark M., 2001, ApJ, 553, 709
- Schade D., Lilly S. J., Crampton D., Ellis R. S., Le Fèvre O., Hammer F., Brinchmann J., Abraham R., Colless M., Glazebrook K., Tresse L., Broadhurst T., 1999, ApJ, 525, 31
- Schechter P., 1976, ApJ, 203, 297
- Spergel, D. N., et al., 2003, ApJ, in press (astro-ph/0302209)
- Sykes C. M., et al., 1998, MNRAS, 301, 310
- Totani T., Yoshii Y., 1998, ApJ, 501, L177
- Treu T., Koopmans L. V. E., 2002, ApJ, 575, 87
- Tully R. B., Pierce M. J., 2000, ApJ, 533, 744
- Turner E. L., 1990, ApJ, 365, L43
- Turner E. L., Ostriker J. P., Gott J. R., III, 1984, ApJ, 284, 1
- van der Marel R. P., 1994, PhD thesis, Leiden University, The Netherlands
- Waddington I., Dunlop J. S., Peacock J. A., Windhorst R. A., 2001, MNRAS, 328, 882
- Wallington S., Narayan R., 1993, ApJ, 403, 517
- White S. D. M., Rees M. J., 1978, MNRAS, 183, 341
- Yasuda N., et al., 2001, AJ, 122, 1104
- Zucca E., et al., 1997, A&A, 326, 477

This paper has been typeset from a \TeX / \LaTeX file prepared by the author.